

## REPORT DOCUMENTATION PAGE

Form Approved  
OMB No. 0704-0188

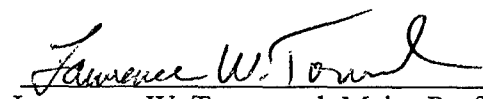
The public reporting burden for this collection of information is estimated to average 1 hour per response, including the time for reviewing instructions, searching existing data sources, gathering and maintaining the data needed, and completing and reviewing the collection of information. Send comments regarding this burden estimate or any other aspect of this collection of information, including suggestions for reducing the burden, to Department of Defense, Washington Headquarters Services, Directorate for Information Operations and Reports (0704-0188), 1215 Jefferson Davis Highway, Suite 1204, Arlington, VA 22202-4302. Respondents should be aware that notwithstanding any other provision of law, no person shall be subject to any penalty for failing to comply with a collection of information if it does not display a currently valid OMB control number.

PLEASE DO NOT RETURN YOUR FORM TO THE ABOVE ADDRESS.

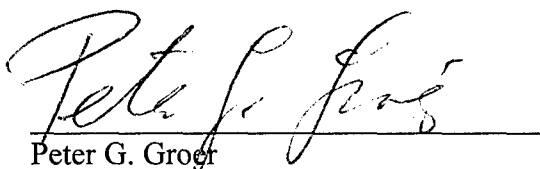
1. REPORT DATE (DD-MM-YYYY) 25/Jun/2001	2. REPORT TYPE THESIS	3. DATES COVERED (From - To)		
4. TITLE AND SUBTITLE COALESCENCE EFFECTS ON NEUTRON PRODUCTION IN HIGH-ENERGY NUCLEUS-NUCLEUS COLLISIONS		5a. CONTRACT NUMBER		
		5b. GRANT NUMBER		
		5c. PROGRAM ELEMENT NUMBER		
6. AUTHOR(S) CAPT BRALEY GERALD S		5d. PROJECT NUMBER		
		5e. TASK NUMBER		
		5f. WORK UNIT NUMBER		
7. PERFORMING ORGANIZATION NAME(S) AND ADDRESS(ES) UNIVERSITY OF TENNESSEE KNOXVILLE			8. PERFORMING ORGANIZATION REPORT NUMBER CI01-109	
9. SPONSORING/MONITORING AGENCY NAME(S) AND ADDRESS(ES) THE DEPARTMENT OF THE AIR FORCE AFIT/CIA, BLDG 125 2950 P STREET WPAFB OH 45433			10. SPONSOR/MONITOR'S ACRONYM(S)	
			11. SPONSOR/MONITOR'S REPORT NUMBER(S)	
12. DISTRIBUTION/AVAILABILITY STATEMENT Unlimited distribution In Accordance With AFI 35-205/AFIT Sup 1				
13. SUPPLEMENTARY NOTES				
14. ABSTRACT				
20010720 026				
15. SUBJECT TERMS				
16. SECURITY CLASSIFICATION OF: a. REPORT		17. LIMITATION OF ABSTRACT	18. NUMBER OF PAGES 49	19a. NAME OF RESPONSIBLE PERSON 19b. TELEPHONE NUMBER (Include area code)

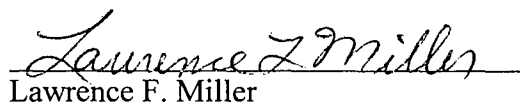
To the Graduate Council:

I am submitting herewith a thesis written by Gerald Scott Braley entitled "Coalescence Effects on Neutron Production in High-Energy Nucleus-Nucleus Collisions." I have examined the final copy of this thesis for form and content and recommend that it be accepted in partial fulfillment of the requirements for the degree of Master of Science, with a major in Nuclear Engineering.

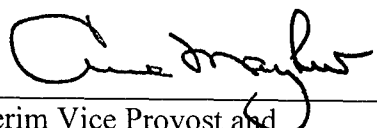
  
\_\_\_\_\_  
Lawrence W. Townsend, Major Professor

We have read this thesis and recommend its acceptance:

  
\_\_\_\_\_  
Peter G. Groer

  
\_\_\_\_\_  
Lawrence F. Miller

Accepted for the Council:

  
\_\_\_\_\_  
Anne Mayhew  
Interim Vice Provost and  
Dean of The Graduate School

COALESCENCE EFFECTS ON NEUTRON PRODUCTION  
IN HIGH ENERGY NUCLEUS-NUCLEUS COLLISIONS

A Thesis  
Presented for the  
Master of Science  
Degree  
The University of Tennessee, Knoxville

Gerald S. Braley  
August 2001

### **Acknowledgements**

The extensive support of Dr. Lawrence W. Townsend, Dr. Laurence Miller, and Dr. Peter Groer is gratefully acknowledged. I further appreciate the opportunity afforded me by the United States Air Force to complete this degree.

## **Abstract**

Reliable methods for accurately predicting neutron production cross sections are needed for a variety of applications including space radiation protection and the use of heavy ion beams in physics and medicine. A three-step model is utilized, including a modified optical model for abrasion and ablation and a coalescence model for neutron removal in the production of deuterons, tritons and other heavier nuclei. Estimates of spectral and angular distributions of neutrons are in good agreement with published cross section measurements.

## Table of Contents

<b>Chapter 1</b>	<b>Introduction</b>	1
	Introduction	1
	Objective of this Work	1
	Organization and Scope of Work	2
<b>Chapter 2</b>	<b>History and Background</b>	3
	History	3
	High-Altitude and Space Radiation	4
	Galactic Cosmic Radiation	4
	Solar Particle Events	6
	Van Allen Belts	6
	Shielding Considerations	7
<b>Chapter 3</b>	<b>Neutron Production Model</b>	8
	Abrasion Theory	8
	Ablation Theory	10
	Coalescence Theory	11
	Parameterization of $\sigma_0$	16
<b>Chapter 4</b>	<b>Results and Discussion</b>	17
	Model Implementation Considerations	17
	Results for Calcium-Hydrogen	18
	Results for Carbon-Aluminum	22
	Results for Neon-Sodium Fluoride	24
<b>Chapter 5</b>	<b>Conclusions and Future Work</b>	26

Conclusions	26
Future Work	26
References	28
Appendix A: Abrasion Theory	32
Appendix B: Coalescence Subroutine	41
Appendix C: Additional Plots, C+Al 75 MeV per nucleon	46
Vita	49

## List of Figures

Figure Title	Page Number
<b>Figure 2.1</b> The energy distribution of charged particles in the space environment	5
<b>Figure 2.2</b> Near-Earth trapped radiation and solar proton environment	7
<b>Figure 4.1</b> Results for Ca+H 357 MeV per nucleon integrated out to 3° lab angle a) Model comparison with data b) Ratios of models vs. experimental data	19
<b>Figure 4.2</b> Results for Ca+H 565 MeV per nucleon integrated out to 3° lab angle a) Model comparison with data b) Ratios of models vs. experimental data c) Angular distribution results	20
<b>Figure 4.3</b> Comparison of results for 75 MeV per nucleon C+Al at 10° lab angle	23
<b>Figure 4.4</b> Comparison of results for 75 MeV per nucleon C+Al at 60° lab angle	23
<b>Figure 4.5</b> Comparison of results for 75 MeV per nucleon C+Al at 125° lab angle, showing the asymptotic behavior of the present model at large lab angles	24
<b>Figure 4.6</b> Comparison of results for 390 MeV per nucleon Ne+Ne at 0° lab angle	25
<b>Figure C.1</b> Comparison of results for 75 MeV per nucleon C+Al at 30° lab angle	47
<b>Figure C.2</b> Comparison of results for 75 MeV per nucleon C+Al at 45° lab angle	48
<b>Figure C.3</b> Comparison of results for 75 MeV per nucleon C+Al at 90° lab angle	48

## List of Symbols

$A$	mass number	$\xi$	defined in equation (A20)
$B$	two-body slope parameter, fm <sup>2</sup>	$\Lambda_n$	defined in equation (A19)
$\mathbf{b}$	impact parameter, fm	$\rho(\mathbf{r})$	one-body density, fm <sup>-3</sup>
$c$	speed of light, m/sec	$\rho(\mathbf{r}, \mathbf{r}')$	one-body density matrix, fm <sup>-3</sup>
$E$	energy, MeV	$\sigma$	cross section, mb
$F$	fragment	$\phi(\mathbf{r})$	single-particle wave function
$F^*$	prefragment	$\chi$	Eikonal phase
$F_l$	probability of emission of ion $l$	$\Psi$	complete nuclear wave function
$f$	scattering operator, fm	$\Omega$	Eikonal inelastic collision term
$g_n$	statistical weight		
$\text{Im}$			Subscripts:
$J_m^{(I)}$	cylindrical Bessel function of the first kind of order $m$	$\text{abl}$	ablation
$K$	projectile target relative wave number, fm <sup>-1</sup>	$\text{abr}$	abrasion
$\mathbf{k}$	wave number of emitted neutrons, fm <sup>-3</sup>	$CN$	formation cross section
$M$	mass, MeV/c	$f$	final state
$m_N$	nucleon mass, MeV/c <sup>2</sup>	$i$	initial state
$N_1$	single-collision term	$j$	abraded nucleons (projectile constituents)
$n$	number of abraded nucleons	$NN$	nucleon-nucleon (two-body)
$n(\mathbf{p})$	momentum distribution	$P$	projectile
$n(\mathbf{x})$	Fourier transform of nucleon momentum distributions	$T$	target
$P$	projectile	$X$	final target state
$\mathcal{P}(\mathbf{b}, \mathbf{b}')$	function describing projectile spectators		
$Q$	defined in equation (A12)		
$\mathbf{q}$	momentum transfer, fm <sup>-3</sup>		
$\mathbf{r}$	internal nuclear coordinate, fm <sup>3</sup>		
$S_n$	separation energy, MeV		
$\mathbf{s}$	transverse part of $\mathbf{r}$		
$T$	target		
$w_0$	level density of residual nucleus		
$X$	final target state		
$z$	component of $\mathbf{r}$		
$\alpha$	ratio or real to imaginary parts of $f_{NN}$		
$\beta$	relative projectile target velocity		
$\Gamma$	profile function		
$\delta$	Dirac delta function		
$\zeta$	target constituent		
$\mu_n$	neutron mass		

## Chapter 1

### Introduction

#### Introduction

The collision of atomic nuclei traveling at or near relativistic speeds with stationary target nuclei produces a shower of nuclear fragments in all directions and at a wide range of energies, including energies significantly higher than those of the original projectile. Sources of these high-energy projectile nuclei include space radiation of cosmic or solar origin, accelerators, and radiation beams used in medical treatment. Of particular concern is the production of secondary neutrons in bulk matter, such as the shielding and components of manned spacecraft or space-based facilities and overlying body tissue that shields underlying organs. Some estimates of dose equivalent for Lunar or Martian base scenarios indicate that up to 50% of the dose equivalent behind thick shields may come from secondary neutrons (Simonsen, 1991). They are also a major source of radiation exposure for flight crews in high-altitude aircraft (NCRP, 1995). Because it is not possible to determine experimentally the neutron production spectra for every possible combination of energy, projectile and target, it is desirable to produce a validated model that can be used to provide cross section predictions as needed for these applications.

#### Objective of This Work

The objective of this work is to further develop existing theories for nucleon production in high-energy nucleus-nucleus collisions, which accurately predict neutron

production cross sections in these reactions. The expanded model will be based on the abrasion-ablation model of Cucinotta, Wilson, and Townsend (Cucinotta, 1997) as extended to include a coalescence model (Nagamiya, 1981), which accounts for the formation of composite particles, such as deuterons, in the debris of these high energy collisions. This model is used to produce spectral and angular cross sections, which are compared to published experimental data.

## **Organization and Scope of Work**

Chapter 2 briefly explains the history and background of heavy ion collisions, as well as the desirability of an accurate model to predict neutron production in these collisions.

Chapter 3 provides details of the theory behind each stage of the model, including modifications and assumptions used to implement the model.

Chapter 4 presents the results of the model and detailed comparisons with prior work and with experimental data.

Chapter 5 contains a summary of this work, a discussion of the advantages and limitations of the model, and a detailed description of work that should be considered in the future.

The appendices include a more rigorous development of the abrasion theory, a copy of the FORTRAN subroutine used to implement the coalescence formalism, and additional tabular and graphical data used in the discussions in Chapter 4.

## Chapter 2

### History and Background

#### History

The first work with high-energy nucleus-nucleus collisions evolved from the study of cosmic radiation. Cosmic radiation was conclusively discovered in 1912, when Victor Hess found that ionizing radiation levels actually increased with altitude, rather than decreasing as had been expected if the source was terrestrial (Moritz, 1963). His balloon-based instruments determined that, at an altitude of 5000 meters, his readings were several times as great as they were at ground level. Initially thought to be high-energy electromagnetic radiation, the radiation was later found to consist of highly energetic charged particles by Jacob Clay. Early studies of nucleus-nucleus collisions were made by setting up targets, often in high altitude balloons or aircraft, and waiting for a suitable incident particle to provide the reaction of interest.

By the 1940's, early work using cyclotrons at Berkeley and Yale, as well as equipment associated with the Manhattan Project began to supplant the use of cosmic-ray targets with the acceleration of carbon and nitrogen ions with kinetic energies as high as 10 MeV per nucleon. Later, more advanced accelerators pushed the available energies and the mass of the accelerated ions to ever-higher levels. Modern accelerators, like the Relativistic Heavy Ion Collider at Brookhaven National Laboratory, are capable of accelerating heavy nuclei (such as gold) up to the 100 GeV per nucleon range.

## High-Altitude and Space Radiation

There are three main sources of radiation hazards to the crews of manned space missions and high-altitude aircraft flights: Galactic cosmic radiation (GCR), solar particle events, and charged particles trapped in the Van Allen Belts. The radiations from these various sources share many characteristics, but each is distinct and must be treated separately.

Figure 2.1 shows the flux densities versus particle energy for charged particles in the space environment. Most of the lower energy particles are protons or electrons, while at very large energies the particles can include much heavier nuclei, as discussed below.

Ideally, sufficient shielding to reduce the dose to reasonable levels would be used to protect crews in space and high-altitude applications. Unfortunately, the cost of boosting large quantities of bulk shielding into orbit or deep space is far too high to be feasible (on the order of \$2000/lb). Hence, more accurate modeling of the radiation environment and its interactions with spacecraft structures will allow designers to optimize the allocation of shielding materials and simultaneously plan mission durations that keep crew doses below applicable limits.

## Galactic Cosmic Radiation

Galactic cosmic radiation consists mainly of fully stripped ions (~98%), with energies up to as high as 1 trillion GeV. The remaining portion (~2%) is made up of electrons and positrons. Of the nuclear portion, about 87 percent is hydrogen, 12 percent is helium, and the remainder is heavier ions. These particles are believed to have their origin in astrophysical phenomena such as novae/supernovae, neutron stars and black holes. The relative abundance of these heavy ions drops fairly steadily with increasing mass up to  $^{56}\text{Fe}$  (~ $10^{-4}$  x the proton flux), and then drops off sharply. Smaller spikes occur

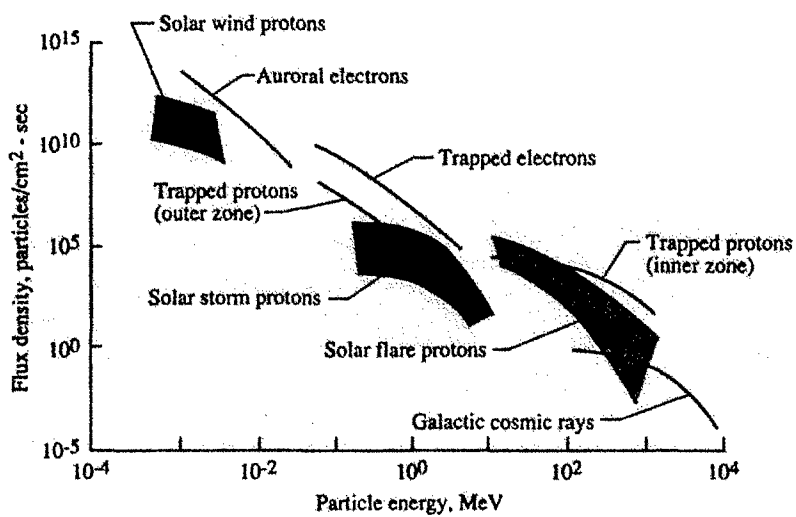


Figure 2.1 The energy distribution of charged particles in the space environment  
(Wilson, 1991)

with carbon and oxygen (both  $\sim 10^{-3}$  x the proton flux). Solar activity and the Earth's magnetic field serve to deflect the lower energy portion of the flux. Typical GCR equivalent doses in low earth orbit (for example, the International Space Station or shuttle missions) are between 20 and 30 mSv/yr. For missions outside the Earth's magnetic field, equivalent doses may be on the order of 40 cSv/yr at solar maximum and 120 cSv/yr at solar minimum (Townsend, 1990).

Secondary neutron production by GCR interactions with the atmosphere and with aircraft parts makes up about half of the total dose equivalent to flight crews and passengers in high-altitude aircraft flights (NCRP, 1995). These doses have been of increasing concern as flight durations increase and the routes are at higher altitudes. Numerous studies have been and are being made to evaluate and predict the risk to flight crews in particular (for example, Chee, 2000; Waters, 2000; Menzel, 2000).

## **Solar Particle Events**

Solar Particle Events (SPE) are injections of high-energy particles into interplanetary space during large disturbances on the sun. The frequency and intensity of these events follow an 11-year cycle and are rare during solar minimum. SPEs are usually associated with solar flares or with coronal mass ejections (CME). They are also somewhat directional in nature; thus, an SPE occurring on the far side of the sun is of little consequence to near-Earth spacecraft from a radiation protection perspective. Most SPEs are either too small or contain too few energetic particles to be of concern to space crews. Extremely large SPEs typically occur only once or twice during a given solar cycle. Near solar maximum, small SPEs occur roughly hourly, while the largest occur monthly.

The spectrum of an SPE can vary quite a bit, but is mainly made up of protons, electrons and alphas with most particle energies below 100 MeV. Heavier ions do not usually contribute a significant portion of the dose.

## **Van Allen Belts**

The Earth is partially shielded from external radiation by its magnetic field. One side effect of these fields is the creation of several “belts” of trapped protons and electrons. Figure 2.2 shows a diagram of the particle distributions. The inner belt is the more stable of the two, and is made up of both high-energy protons with an average energy of 50 MeV and electrons with an average energy of 2 MeV. The outer belt is more diffuse and has mainly lower energy protons and electrons. The most energetic trapped particles are thought to be the result of the decay of neutrons produced by GCR

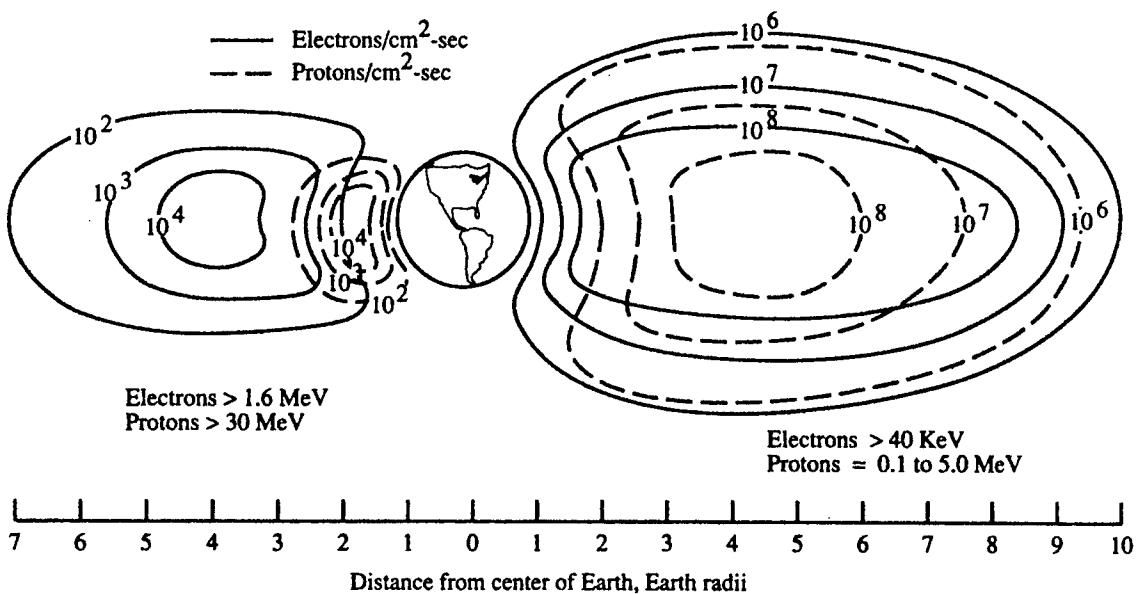


Figure 2.2. Near-Earth trapped radiation and solar proton environment. For clarity, low-energy integral fluxes are shown only on the right, and high-energy fluxes on the left.  
 (Parker and West, 1973)

interacting with the upper atmosphere, while others accumulate from the solar wind, solar particle events, and other sources.

### Shielding Considerations

No human, of course, travels unprotected in space or in the upper atmosphere. Vehicle hulls, protective clothing, equipment, dedicated shielding and self-shielding all provide a measure of protection from the radiation environment. These same shields, however, accentuate the need for accurate models of neutron production in high-energy particle collisions. The typical shielding assumed for a spacecraft without dedicated radiation shielding is  $5 \text{ g/cm}^2$  of aluminum. Plans for long-duration space missions include provision of a “storm shelter” with  $18$  to  $24 \text{ g/cm}^2$  of aluminum for use during SPEs (Simonsen, 1991).

## Chapter 3

### Neutron Production Model

Particle production in high-energy nucleus-nucleus collisions is considered to come from two stages: first, nucleons are sheared off (abraded) during collision, then the remaining, excited pieces of the projectile and target decay by particle and gamma emission.

The present model includes the abrasion (knockout) step, the ablation step, and then adds a coalescence step. Previous versions of these models (Cucinotta, 1997) applied the abrasion (knockout) portion to both the projectile and the target and ablation to the projectile only, but did not incorporate a coalescence step. Incorporating coalescence is the major new feature of this work. In the abrasion stage, a Glauber model is used that incorporates effects of final-state interaction (Glauber, 1970). A more detailed derivation of the abrasion model due to Cucinotta (Cucinotta, 1997) appears as Appendix A. The ablation stage uses a classical evaporation model (Cucinotta, 1994a; Weisskopf, 1940) to evaluate the decay of the remaining portions (called prefragments) of the target and projectile nuclei. Finally, the coalescence stage uses a modified version of an existing model (Nagamiya, 1981) to include particles emitted by the projectile as well as the target.

#### Abrasion Theory

In an abrasion-ablation model the momentum distribution of the nucleons produced by the collision is given by

$$\left( \frac{d\sigma}{d\mathbf{k}} \right) = \left( \frac{d\sigma}{d\mathbf{k}} \right)_{abr} + \left( \frac{d\sigma}{d\mathbf{k}} \right)_{abl} \quad (1)$$

In the Glauber model the scattering amplitude for knockouts is related to the phase space of each particle appearing in the final state. Neutrons produced by this model are considered to originate in the projectile rest frame; by exchanging the target and projectile and converting to the target rest frame (lab frame), values for the target can be obtained. Using a single momentum vector denoted as  $\mathbf{p}_x$  to apply closure to the target final state, the cross section is given by

$$d\sigma = \frac{(2\pi)^4}{\beta} \sum_X d\mathbf{p}_X d\mathbf{p}_{F^*} \sum_{n=1}^n \prod_{j=1}^n [d\mathbf{p}_j] \delta(E_i - E_f) \delta(\mathbf{p}_i - \mathbf{p}_f) |T_{fi}|^2 \quad (2)$$

where  $\beta$  is the relative projectile velocity divided by the speed of light,  $F^*$  represents the prefragments,  $n$  is the number of nucleons knocked out of the projectile in the collision with the target,  $T$  is the transition amplitude that describes the collision, and  $i$  and  $f$  denote the initial and final states, respectively. Using a Glauber model for the transition amplitude ( $T$ ) in equation (2), along with closure on the target states, allows the momentum distribution from abrasion to be written as

$$\left( \frac{d\sigma}{d\mathbf{k}} \right)_{abr} \approx \sum_n \binom{A_p}{n} \int d^2 b \mathcal{P}^{A_p-n}(\mathbf{b}) \frac{dN_n}{d\mathbf{k}} \quad (3)$$

where  $A_p$  is the projectile mass number,  $\mathcal{P}^{A_p-n}(\mathbf{b})$  denotes the probability that  $A_p - n$  nucleons are not removed by knockout at impact parameter  $\mathbf{b}$ , and the distribution of knockouts versus impact parameter is given by  $dN_n/d\mathbf{k}$ . The latter can be written in terms of single collision terms  $dN_1/d\mathbf{k}$  as

$$\frac{dN_n}{d\mathbf{k}} = \frac{dN_1}{d\mathbf{k}} [1 - \mathcal{P}(\mathbf{b})]^{n-1} \quad (4)$$

In the optical limit, we have

$$\mathcal{P}(\mathbf{b}) = \exp\left[-\frac{2 \operatorname{Im} \chi(\mathbf{b})}{A_p}\right] \quad (5)$$

where the eikonal phase  $\chi$  is given in terms of one-body form factors  $F(\mathbf{q})$  for the projectile and target and the nucleon scattering amplitude  $f_{NN}$  as

$$\chi(\mathbf{b}) = \frac{A_p A_T}{(2\pi k_{NN})} \int d^2 q \exp(i\mathbf{q} \cdot \mathbf{b}) F_p(q) F_T(q) f_{NN}(q) \quad (6)$$

with  $A_T$  as the target mass number and  $\mathbf{q}$  denoting the momentum transfer in the collision. The form factor  $F(q)$  is the Fourier transform of the appropriate (projectile or target) nuclear density.

### Ablation Theory

After the projectile-target collision, a distribution of compound (prefragment) nuclei in various states of excitation remains. The excitation spectrum is treated as an average state in the abrasion-ablation model, with a single or small number of average excitation energies used to describe the prefragment and the strength of the state determined by the total abrasion cross section. Next, estimate the average excitation energies and calculate the neutron spectrum from ablation with the Weisskopf-Ewing statistical decay model. Define  $P_n(j, \mathbf{k})$  as the probability that a prefragment labeled  $j$  with mass number  $A_j$ , charge number  $Z_j$ , and excitation energy  $E_j^*$ , emits a neutron of momentum  $\mathbf{k}$  (Weisskopf, 1940; Kikuchi, 1968). The momentum distribution for neutron production from ablation in the projectile rest frame is written as:

$$\left( \frac{d\sigma}{d\mathbf{k}} \right)_{\text{abl}} = \sum_j \sigma_{\text{abr}}(A_j, Z_j, E_j^*) P_n(j, \mathbf{k}) \quad (7)$$

The total abrasion cross section in equation (7) is evaluated from the abrasion momentum distribution in equation (3).

In the statistical model, the prefragment (compound nucleus) is assumed to be infinitely heavy, and the emission spectrum is assumed to be isotropic in the rest frame. The probability function, as given in (Weisskopf, 1940; Kikuchi, 1968), is

$$P_n(j, E_n) = \frac{2\mu_n g_n E_n \sigma_{CN} w_o (E_j^* - E_n)}{\sum_l F_l} \quad (8)$$

where  $\mu_n$  is the reduced neutron mass,  $g_n$  is the statistical weight,  $\sigma_{CN}$  is the formation cross section by the inverse process,  $w_o$  is the level density of the residual nucleus, and

$$F_l = \int_0^{E_j^* - S_j} P_l(j, E) dE \quad (9)$$

Competition occurs between the emission of the light particles  $n$ ,  $p$ ,  $^2H$ ,  $^3H$ ,  $^3He$ , and  $\alpha$ . The model parameters are taken from (Dostrovsky, 1959). If sufficient excitation energy is available, then several neutrons will be emitted. The cumulative spectrum is

$$P_n(j, E_n) = P_n(j, E_n) + \sum_l \int_0^{E_j^*} P_l(j, E_l) P_n(k, E_n) dE_l + \dots \quad (10)$$

In this work, terms through the third order in the series of equation (10) are considered. The neutron momentum distribution in the lab frame is found by multiplying equation (7) by the appropriate neutron energy to form a Lorentz invariant and then performing the transformation to the laboratory system.

### Coalescence Theory

The abrasion and ablation models presented thus far yield single particles with a forward-peaked distribution. Certain of these particles, with similar momenta, may

coalesce to form heavier nuclei, such as deuterons, tritons, helions, and alphas. Schwartschild and Zupančič (Schwartzschild, 1963) predicted that the deuteron density in momentum space is proportional to the proton density times the probability of finding a neutron within a small sphere of radius  $p_0$  around the proton momentum. Following Awes (Awes, 1981), the probability  $P$  of finding a single nucleon in the coalescence volume centered at a momentum per nucleon  $\mathbf{p}$  is given by the product of this volume ( $\frac{4\pi}{3} p_0^3$ ) with the single nucleon momentum density

$$P = \frac{4\pi}{3} p_0^3 \frac{\gamma}{m} \frac{d^3 N(\mathbf{p})}{dp^3} \quad (11)$$

where  $d^3 N(\mathbf{p})/dp^3$  represents the differential nucleon multiplicity,  $\bar{m}$  is the average nucleon multiplicity, and  $\gamma = 1 + T/m$ . For  $\gamma$  only,  $m$  is the nucleon mass, rather than the multiplicity. This is simply the volume times the number of nucleons per unit volume, all in momentum space.

For a given multiplicity  $m$ , such as when  $m$  nucleons are produced in an event, the probability of finding  $n$  of them ( $n \leq m$ ) in the coalescence volume will be given by the binomial distribution

$$P(n|m) = \binom{m}{n} P^n (1-P)^{m-n} \quad (12)$$

Each multiplicity will have a probability  $f(m)$  of occurrence, which can be summed over the distribution of multiplicities to obtain the mean probability for finding  $n$  nucleons in the coalescence volume.

$$\langle P(n) \rangle = \sum_{m \geq n} f(m) P(n|m) = \sum_{m \geq n} f(m) \binom{m}{n} P^n (1-P)^{m-n} \quad (13)$$

In the case of low average multiplicities, it is reasonable to assume a Poisson distribution of multiplicities

$$f(m) = \frac{(\bar{m})^m}{m!} e^{-\bar{m}} \quad (14)$$

which can be substituted into equation (13) which gives

$$\begin{aligned} \langle P(n) \rangle &= \sum_{m \geq n} \frac{(\bar{m})^m}{m!} e^{-\bar{m}} \frac{m!}{n!(m-n)!} P^n (1-P)^{m-n} \\ &= \frac{(\bar{m}P)^n e^{-\bar{m}}}{n!} \sum_{\nu \geq 0} \frac{1}{\nu!} [(1-P)\bar{m}]^\nu \\ &= \frac{(\bar{m}P)^n e^{-\bar{m}P}}{n!} \end{aligned} \quad (15)$$

which is exact for a Poisson multiplicity distribution. At relativistic energies large multiplicities are observed with a non-Poisson distribution, in which case it is assumed that equation (13) can be approximated by

$$\langle P(n) \rangle \approx P(n|\bar{m}) = \binom{\bar{m}}{n} P^n (1-P)^{\bar{m}-n} \quad (16)$$

Then if  $P \ll 1$  and  $\bar{m} \gg n$  the binomial distribution becomes Poisson in form, which again results in equation (15).

Since  $\bar{m}P$  is quite small, the exponential term in equation (15) can be ignored, which means that the average probability for having  $N$  neutrons and  $Z$  protons in the coalescence sphere is

$$\langle P(N, Z) \rangle = \frac{(\bar{m}_Z P_Z)^Z}{Z!} \frac{(\bar{m}_N P_N)^N}{N!} \quad (17)$$

where it is assumed that the probabilities for the presence of neutrons and protons are independent. In this context,  $P(N, Z)$  represents the probability of forming a composite particle with the momentum per nucleon  $\mathbf{p}$ .

Substituting equation (11) into equation (17) and dividing by the coalescence volume gives the composite particle momentum distribution in the form of the coalescence relation used at relativistic energies

$$\frac{d^3 N(Z, N)}{dp^3} = \left( \frac{Z_t + Z_p}{N_t + N_p} \right)^Z \frac{1}{N! Z!} \left( \frac{4\pi}{3} p_0^3 \gamma \right)^{A-1} \left( \frac{d^3 N(0,1)}{dp^3} \right)^A \quad (18)$$

where  $Z$ ,  $N$ , and  $A$  are the composite particle charge, neutron number and mass respectively;  $N_p$  and  $N_t$  are the projectile and target neutron numbers, and  $Z_p$  and  $Z_t$  are the projectile and target charge numbers. The multiplicity is related to the momentum distributions by

$$\frac{d^3 N}{dp^3} = \frac{1}{\sigma_0} \frac{d^3 \sigma}{dp^3} \quad (19)$$

The quantity  $\sigma_0$  is the projectile-target total reaction cross section, and is calculated using one of two formulations, described below. Applying equation (19), we obtain

$$\frac{d^3 \sigma(Z, N)}{dp^3} = \left( \frac{Z_t + Z_p}{N_t + N_p} \right)^Z \frac{1}{N! Z!} \left( \frac{4\pi p_0^3 \gamma}{3\sigma_0} \right)^{A-1} \left( \frac{d^3 \sigma(0,1)}{dp^3} \right)^A \quad (20)$$

Since, as part of the abrasion and ablation steps, we obtain Lorentz invariant cross sections for the total neutron production, we want to convert this to utilize  $\sigma_l(n)$ , the

invariant neutron cross section. The invariant cross section is related to the triple

differential cross section by  $\frac{d^3\sigma}{dp^3} = \frac{1}{E} \sigma_I$ . Substituting into equation (20), we get

$$\frac{1}{E_A} \sigma_I(A) = \underbrace{\left( \frac{Z_I + Z_p}{N_I + N_p} \right)^Z}_{C_T} \frac{1}{N! Z!} \left( \frac{4\pi p_0^3 \gamma}{3\sigma_0} \right)^{A-1} \left( \frac{1}{E} \sigma_I(n) \right)^A \quad (21)$$

$$\sigma_I(A) = \frac{E_A C_T}{E^A} [\sigma_I(n)]^A \quad (22)$$

but  $E_A = AE \Rightarrow \frac{E_A}{E^A} = \frac{EA}{E^A} = \frac{A}{E^{A-1}}$  so

$$\sigma_I(A) = \frac{AC_T}{E^{A-1}} [\sigma_I(n)]^A \quad (23)$$

which yields

$$\sigma_I(Z, N) = \left( \frac{Z_I + Z_p}{N_I + N_p} \right)^Z \frac{A}{N! Z!} \left( \frac{4\pi p_0^3 \gamma}{3\sigma_0 E} \right)^{A-1} (\sigma_I(n))^A \quad (24)$$

but  $\frac{\gamma}{E} = \frac{1 + \frac{T}{m}}{T + m} = \frac{1}{m}$ , the inverse of the nucleon rest mass energy. Thus,

$$\sigma_I(Z, N) = \left( \frac{Z_I + Z_p}{N_I + N_p} \right)^Z \frac{A}{N! Z!} \left( \frac{4\pi P_0^3}{3\sigma_0 m} \right)^{A-1} (\sigma_I(n))^A \quad (25)$$

Nagamiya et. al. rewrote equation (25) in a slightly different form by using a constant, energy-independent coalescence coefficient  $C_A$  in an equation of the form

$$E_A \left( \frac{d^3\sigma_A}{dp_A^3} \right) = C_A \left( E \left( \frac{d^3\sigma_p}{dp_p^3} \right) \right)^A \quad (26)$$

where  $p_A = Ap_p$  and  $A$  is the mass of the coalesced fragment. Comparing equation (26) with equation (21), we can see that  $C_A$  is comparable to our  $C_T$ , which is also energy and angle independent.

### Parameterization of $\sigma_0$

For nucleon-nucleus reactions, a parameterization by Wilson (Wilson, 1988) was used,

$$\sigma_0 = 45f(E)A^{0.7}\{1 + 0.016\sin[5.3 - 2.63\ln(A)]\} \quad (27)$$

where  $A$  is the mass number of the target nucleus and the energy-dependent factor is

$$f(E) = 1 - 0.62 \exp(-E/200) \sin(10.9E^{-0.28}) \quad (28)$$

with the incident kinetic energy  $E$  in units of MeV/nucleon.

For nucleus-nucleus reactions, a different parameterization was used (Townsend, 1986),

$$\sigma_0 = \pi r_0^2 \beta(E) [A_p^{1/3} + A_T^{1/3} - \delta(A_p, A_T, E)]^2 \quad (29)$$

with

$$\beta(E) = 1 + 5E^{-1} \quad (30)$$

and

$$\delta(A_p, A_T, E) = 0.200 + \left(\frac{1}{A_p}\right) + \left(\frac{1}{A_T}\right) - 0.292 \exp(-E/792) \cos(0.229E^{0.453}) \quad (31)$$

with  $r_0 = 1.26$  fm and  $E$  again in units of MeV/nucleon.

## Chapter 4

### Results and Discussion

In order to determine the accuracy and validity of this neutron production model, a comparison with experimental data is conducted for four interactions: 357 MeV/A Ca+H (Tuve, 1997), 565 MeV/A Ca+H (Tuve, 1997), 75 MeV/A C+Al (Heilbronn, unpublished), and 390 MeV/A Ne+Ne (Madey, 1985).

#### Model Implementation Considerations

The implementation of the complete model consists of about 2800 lines of FORTRAN 77 code, which was developed and run on a DEC Personal Workstation 433a, compiled with Compaq Fortran for Alpha Linux v1.0 and run on RedHat Linux v7.0. Results were transferred to Microsoft Excel 2000 for plotting and statistical analysis. The subroutine calculating coalescence, the major contribution to this model in this work, is included in appendix B.

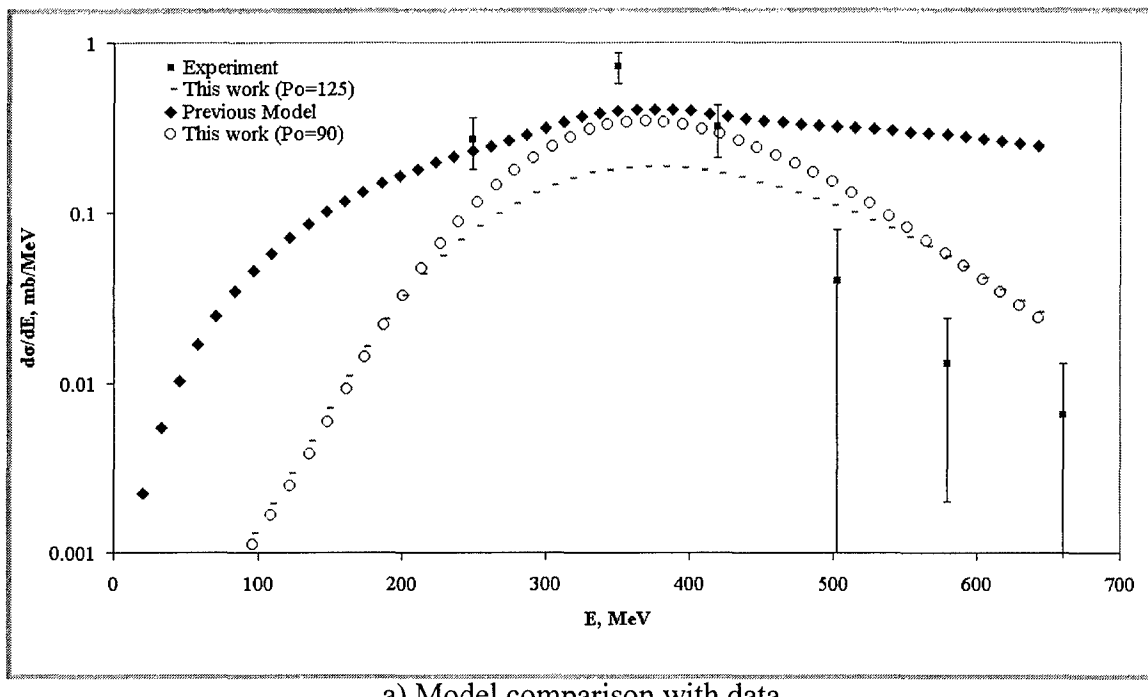
As with any computer model of such complexity, some numerical problems can creep in to the code. Roundoff error is the most common trouble. For example, at one place in the ablation code, the numerator and denominator of a particular expression were supposed to proceed “in step” to 0. L’Hopital’s rule analytically showed the limit to be 0; however, roundoff error generated a result where some of the cross sections at small angles behaved like  $\lim_{x \rightarrow 0} (1/x)$ . This was corrected by numerical interpolation from the surrounding cross section estimates.

Another numerical problem was that the code that modeled the abrasion behavior of the target produced results which behaved asymptotically at large lab angles and eventually dominated the overall spectrum. This problem has not been corrected at present and remains for future work.

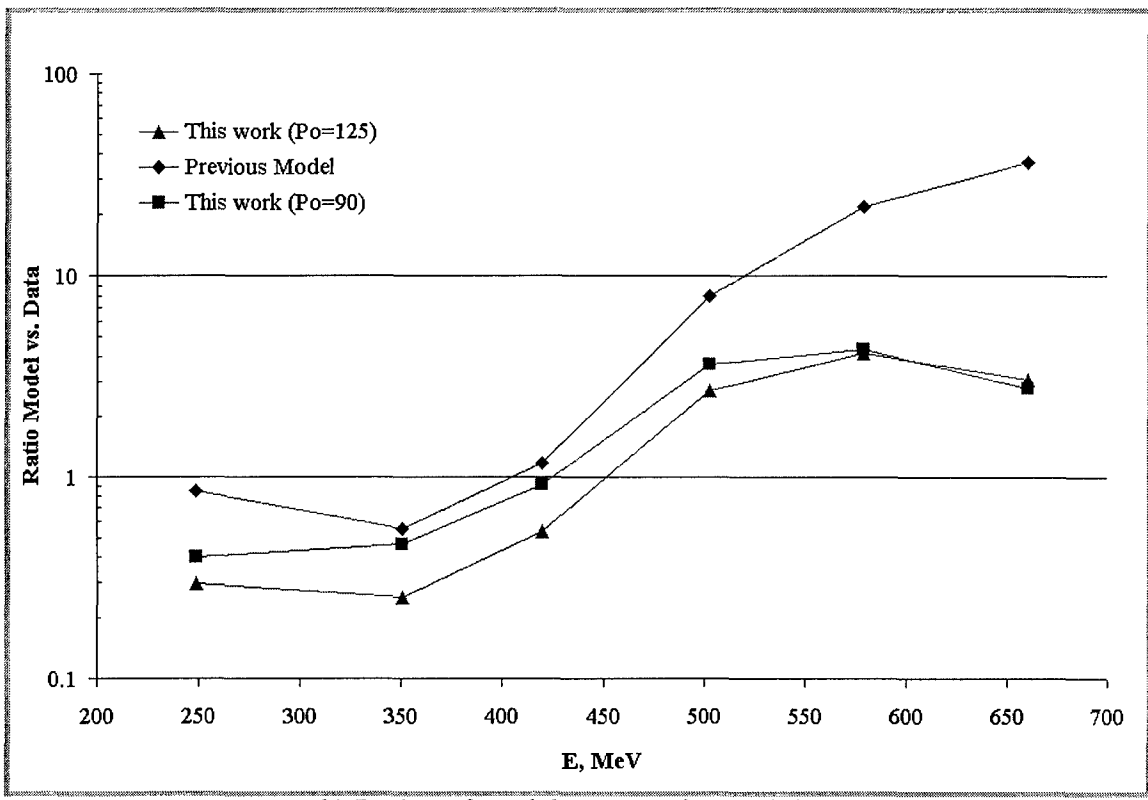
As discussed in the previous chapter, the coalescence step of the present model depends on the selection of a single parameter,  $p_0$ , the coalescence radius. A wide range of values for  $p_0$  has been proposed; some authors propose different values for each composite particle formed. Awes et al., for example, proposed values of 170 MeV/c, 215 MeV/c, and 270 MeV/c for deuterons, tritons, and alphas respectively (Awes, 1981). Gutbrod et al. proposed values ranging from 106 to 147 MeV/c for a range of interactions (Gutbrod, 1976). Nagamiya et al., whose results were most influential on the present work, selected a single value of 90 MeV/c and obtained very good agreement with their data (Nagamiya, 1981). For the purposes of comparison, results here are presented with values for  $p_0$  of 90 MeV/c and 125 MeV/c, the latter being representative of the values found by Gutbrod et al.

### **Results for Calcium-Hydrogen**

Figures 4.1 (a and b) and 4.2 (a, b, and c) display the results obtained for 357 and 565 MeV per nucleon calcium projectiles on hydrogen targets integrated out to  $3^\circ$  from the beam angle. The figures also include the results obtained with the earlier version (Cucinotta, 1997) of the current model, prior to the inclusion of coalescence. As these figures demonstrate, the current work fits the high energy portion of the spectrum much more closely than the previous model, although the high-energy portion still tends to be

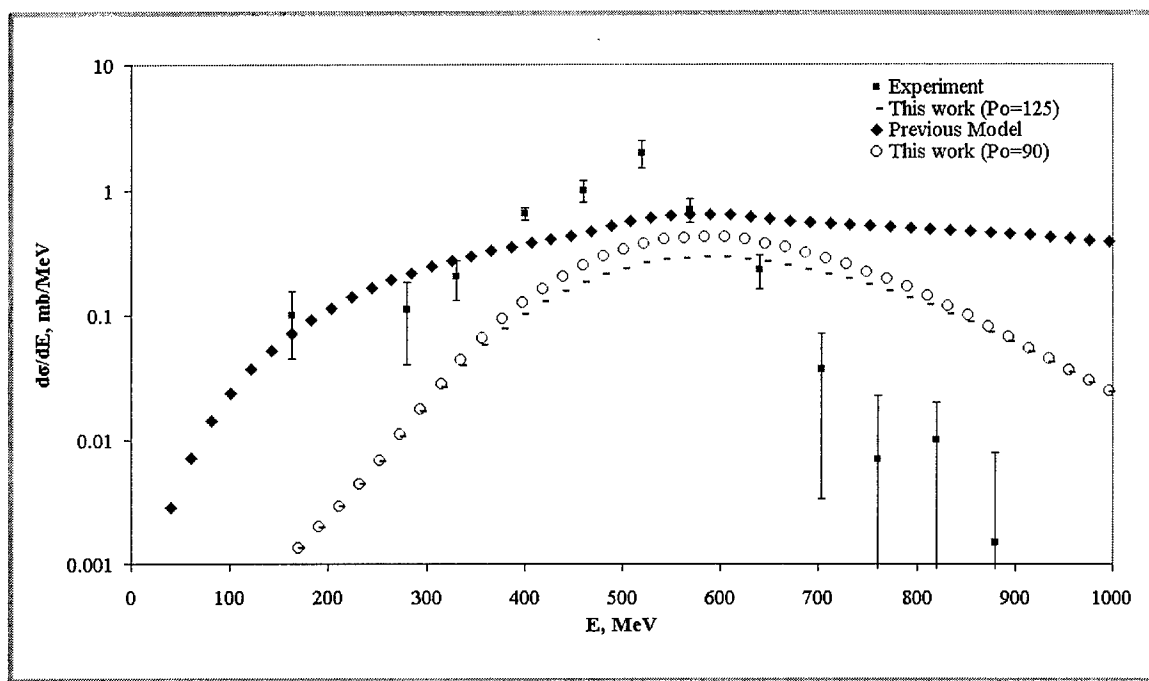


a) Model comparison with data

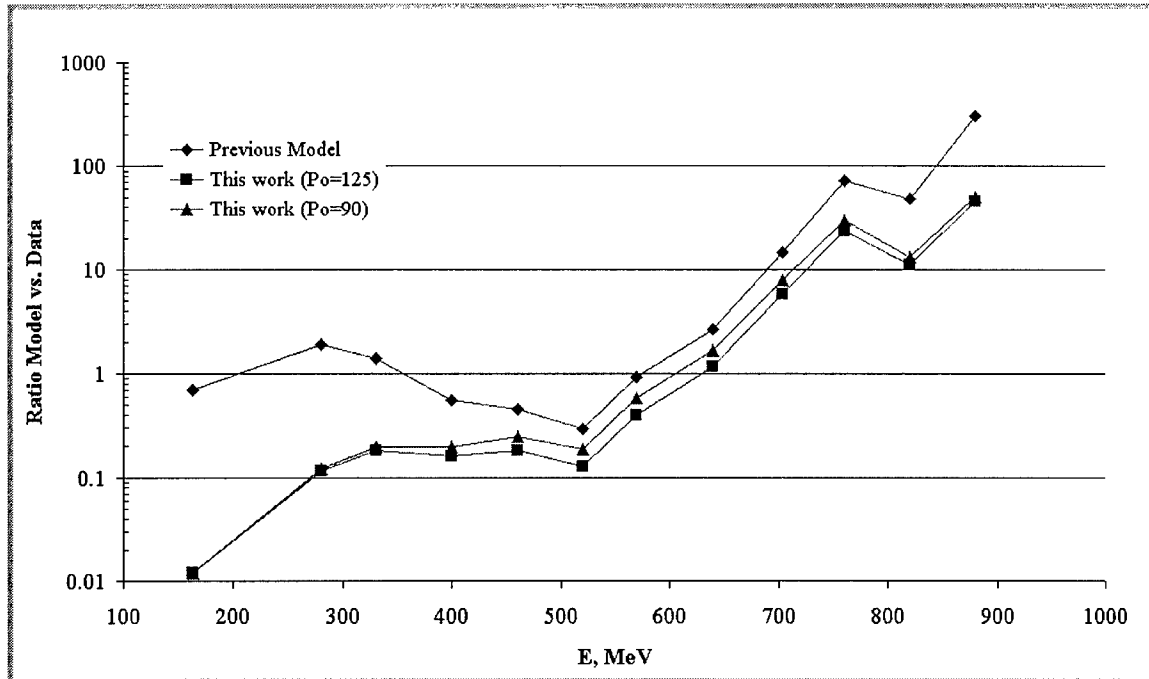


b) Ratios of model vs. experimental data

Figure 4.1 Results for Ca+H 357 MeV per nucleon integrated out to 3° lab angle

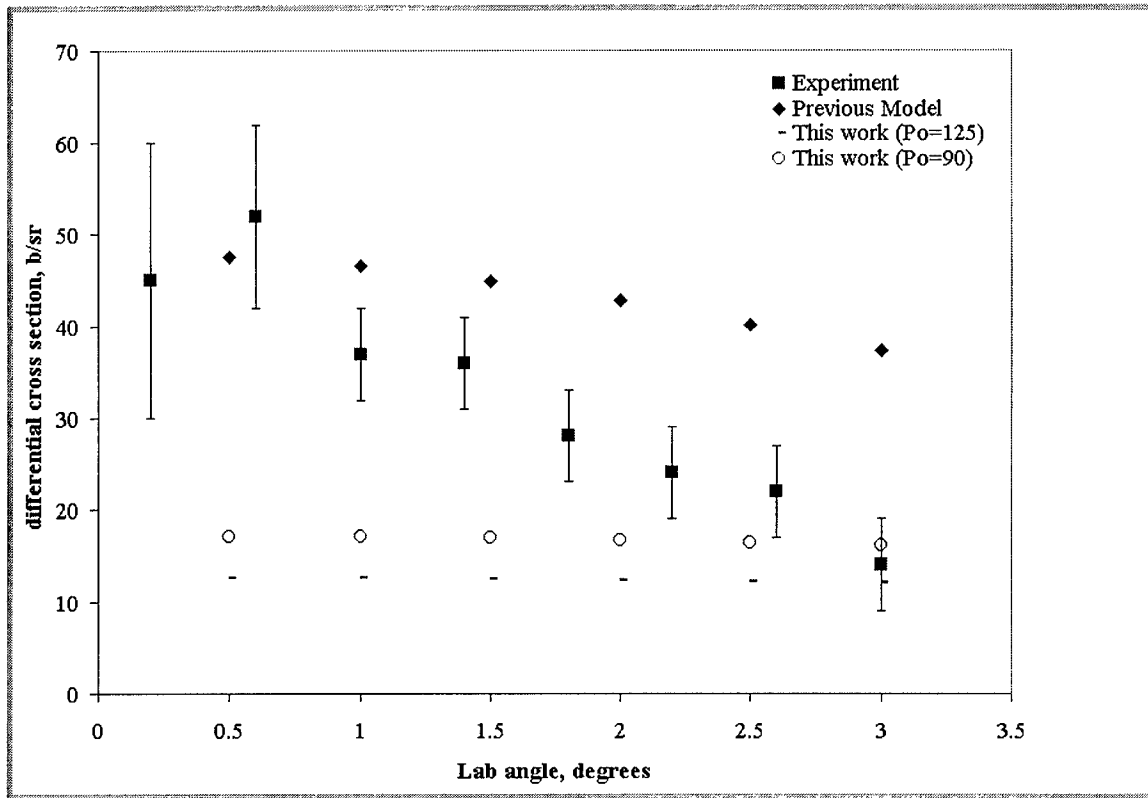


a) Model comparison with data



b) Ratios of models vs. experimental data

Figure 4.2 Results for Ca+H 565 MeV per nucleon integrated out to  $3^\circ$  lab angle



c) Angular distribution results

Figure 4.2 continued

Table 4.1 Chi-squared goodness of fit check for previous and current models. Bold type indicates best fit.

Beam Energy T (MeV per nucleon)	$\chi^2$ E < T	$\chi^2$ E > T	$\chi^2$ All E
357 Previous Model	<b>4.91</b>	128.79	133.70
357 This Work, $p_0 = 125$ MeV/c	17.33	<b>5.90</b>	23.23
357 This Work, $p_0 = 90$ MeV/c	9.86	8.39	<b>18.25</b>
565 Previous Model	<b>769.0</b>	8449.0	9218.0
565 This Work, $p_0 = 125$ MeV/c	1759.4	<b>340.2</b>	2099.6
565 This Work, $p_0 = 90$ MeV/c	1491.9	491.0	<b>1982.9</b>

overestimated. Since prior model data was available for these projectile-target combinations, a chi-squared test was made, with the results in table 4.1 below.

Both the figures and the table above demonstrate that, for both of these projectile-target combinations, using a  $p_0$  of 90 MeV/c is a better choice than 125 MeV/c. Both choices were a better fit to the energy spectrum above the beam energy than was the previous model, but the previous model was a better fit below the beam energy. Figure 4.2c, the angular distribution, shows that none of the models predicts a sufficient falloff with increasing angle. It should be noted that, for the 357 MeV per nucleon, there were only two experimental data points below the beam energy, making the comparison somewhat weak. Overall, the current model with a  $p_0$  of 90 MeV/c is the best fit at both 357 MeV per nucleon and at 565 MeV per nucleon. Better low-energy data for these projectile-target combinations would help clarify the situation.

### Results for Carbon-Aluminum

Figures 4.3, 4.4 and 4.5 compare the results for 75 MeV per nucleon carbon projectiles on aluminum targets at 10, 60 and 125 degrees. Appendix C contains additional figures for 30, 45, and 90 degrees. Several aspects of these figures warrant discussion. As the experimental data are recent and unpublished (Heilbronn, private communication), they have been arbitrarily scaled so that, at each lab angle, the maximum experimental value is 1.0. Also, because the experimental data analyses are not yet complete, the final values may change. Figures 4.4, and, in particular, 4.5 demonstrate the problem of asymptotic behavior in the target knockout portion of the code.

A statistical analysis comparing the  $\chi^2$  values for  $p_0 = 90$  MeV/c and for

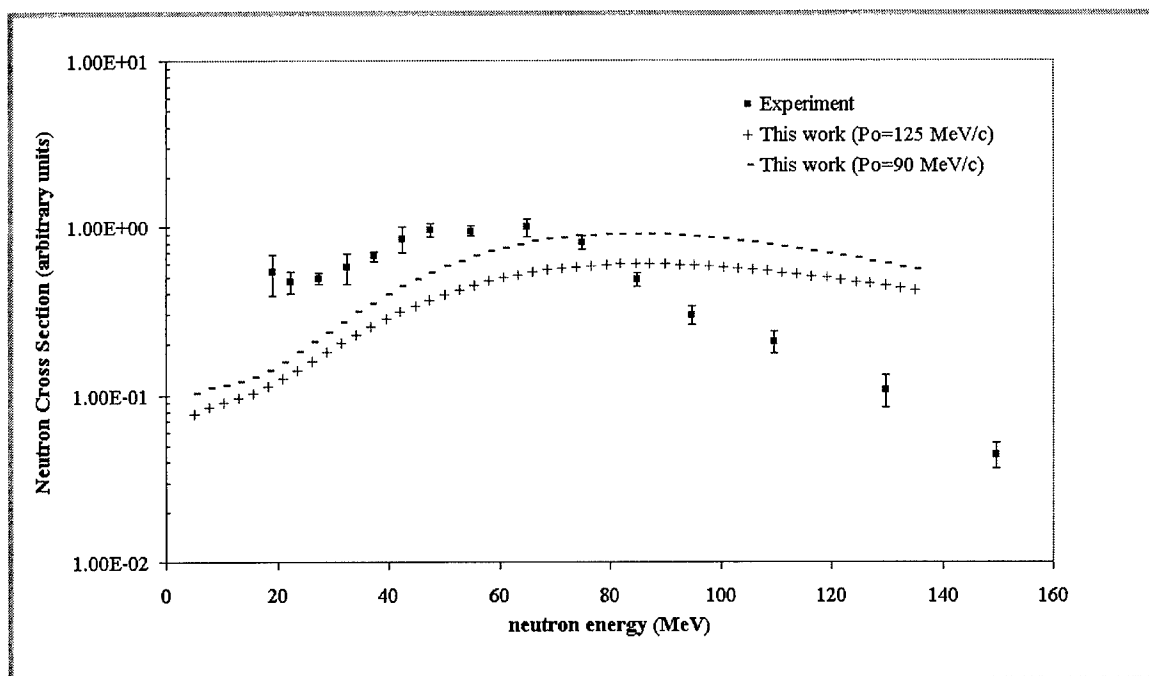


Figure 4.3 Comparison of results for 75 MeV per nucleon C+Al at 10° lab angle

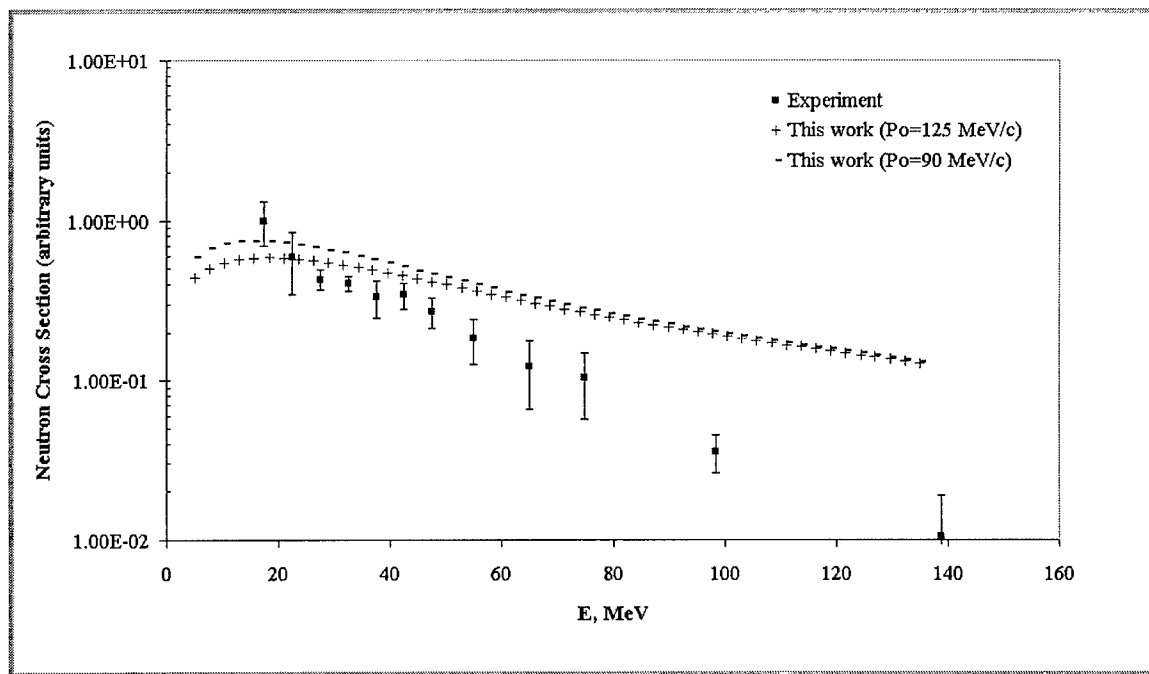


Figure 4.4 Comparison of results for 75 MeV per nucleon C+Al at 60° lab angle

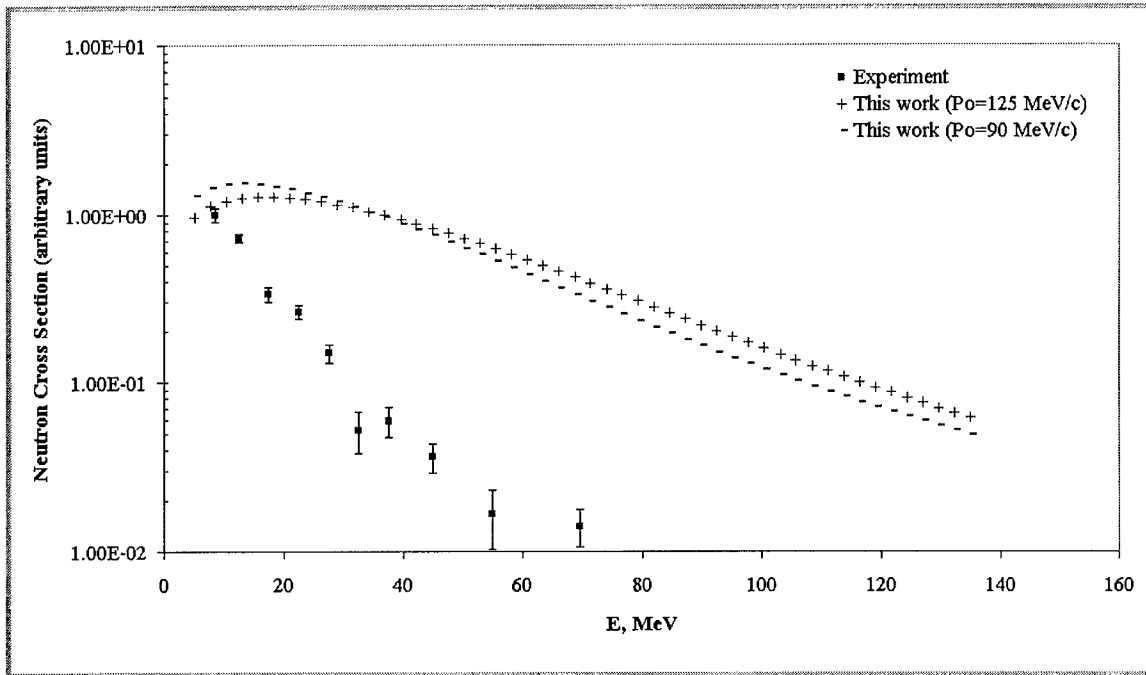


Figure 4.5 Comparison of results for 75 MeV per nucleon C+Al at 125° lab angle, showing the asymptotic behavior of the present model at large lab angles.

$p_0 = 125$  MeV/c (included in appendix C) shows that 125 gives the better fit for all but the 125° data; however, above 60 degrees the fit is too poor to be significant.

### Results for Neon-Sodium Fluoride

Figure 4.6 shows the results obtained for 390 MeV per nucleon neon projectiles on sodium fluoride targets at a 0° lab angle. For this model, experimental data for Ne-NaF was compared with computed results for Ne-Ne, which is nearly the same for analysis purposes. Because numerical values for the experimental data uncertainties were not available, no formal statistical analysis was made. However, it is clear from the plot that the selection of  $p_0 = 90$  MeV/c is the better choice for this projectile-target combination. In this case, as well, the underestimation at the low energies is quite evident, as is the smaller overestimation at high energies.

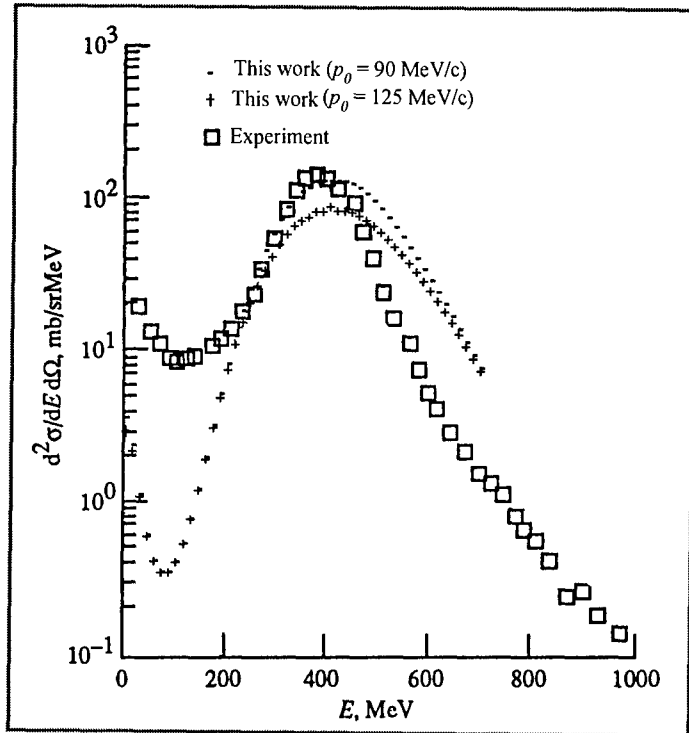


Figure 4.6 Comparison of results for 390 MeV per nucleon Ne+Ne at  $0^\circ$  lab angle

## Chapter 5

### Conclusions and Future Work

#### Conclusions

The expanded model described in the preceding chapters provides a fairly good fit to published data, although further development is needed. In most of the cases considered, the addition of coalescence and the target ablation provided a better fit than the previous model, with the selection of 90 MeV/c for the coalescence radius generally yielding the best results. The good agreement between the model and published experimental data suggests that significant progress has been made in developing an accurate tool to predict neutron spectra from heavy ion collisions.

#### Future Work

Three code-specific problems need to be addressed. The first, already mentioned in chapter 4, is to provide a better solution to the problem of the cross section becoming infinite at energies very close to the beam energy for very small lab angles. The linearization already implemented in the code should either be replaced by an appropriate curve fit or a better approximation for the analytical expression should be found.

Second, a better formulation for the target abrasion model should be developed. The present code yields cross sections that behave asymptotically at large lab angles, whereas the cross sections should be dropping to 0 at higher energies. The values involved in the calculations are small enough that roundoff error may be involved.

Third, due to inherent limitations in the way FORTRAN 77 assigns array sizes, the code is currently restricted to a maximum nucleus mass (target or projectile) of 68.

Recasting the code into a newer version of FORTRAN would enable array sizes to be dynamically assigned, and would remove this limitation.

Aside from code modifications, further research is needed to select a better value for the coalescence radius  $p_0$ , or a parameterization if a single value is not appropriate. As one might expect, the larger the value chosen the larger the number of nucleons that coalesce to product light nuclei. For most of the cases considered herein,  $p_o = 90$  MeV/c gave a good fit to the experimental data, but not in every case. The values in the literature vary greatly with projectile and target masses, beam energies, and type of composite fragment formed.

Also desirable would be more detailed data concerning the low energy neutron spectrum to help determine the accuracy of the model in this region.

Once a fully acceptable model has been produced, a database of neutron production cross sections for a wide range of projectile-target and energy combinations can be developed for use in accurately predicting doses from cosmic radiation and large solar particle events. The model can also be used to predict light ion production cross sections produced by the coalescence step.

## **References**

Awes, T.C.; Poggi, G.; Gelbke, C.K.; Back, B.B.; Glagola, B.G.; Breuer, H.; Viola, V.E. "Precompound emission of light particles in the reaction  $^{16}\text{O} + ^{238}\text{U}$  at 20 MeV/nucleon," *Physical Review C*, **24**, 89 (1981)

Chee, P.A.; Braby, L.A.; Conroy, T.J. "Potential Doses to Passengers and Crew of Supersonic Transports", *Health Physics*, **79**, 547 (2000)

Cucinotta, F.A.; Townsend, L.W.; Wilson, J.W. "Inclusive Inelastic Scattering of Heavy Ions in the Independent Particle Model," *Journal of Physics G: Nuclear Particle Physics*, **18**, 889 (1992)

Cucinotta, F.A. "Forward Production of Protons in Relativistic  $^{12}\text{C}$ -Nucleus Collisions," *Journal of Physics G: Nuclear Particle Physics*, **20**, 1803 (1994a)

Cucinotta, F.A. "Multiple-Scattering Model for Inclusive Proton Production in Heavy Ion Collisions," NASA Technical Paper No. TP-3470 (1994b)

Cucinotta, F.A.; Wilson J.W.; Townsend, L.W. "Abrasion-ablation model for neutron production in heavy ion collisions," *Nuclear Physics A*, **619**, 202 (1997)

Dostrovsky, I.; Fraenkel, Z.; Friedlander, G. "Monte Carlo Calculations of Nuclear Evaporation Processes. III. Applications to Low-Energy Reactions," *Physical Review*, **116**, 638 (1959)

Glauber, R.J.; Matthiae, G. "High-Energy Scattering of Protons by Nuclei", *Nuclear Physics*, **B21**, 135 (1970)

Gutbrod, H.H.; Sandoval, A.; Johansen, P.J.; Poskanzer, A.M.; Gosset, J.; Meyer, W.G.; Westfall, G.D.; Stock, R. "Final-State Interactions in the Production of Hydrogen and Helium Isotopes by Relativistic Heavy Ions on Uranium," *Physical Review Letters*, **37**, 667 (1976)

Haneishi, Y.; Fujita, T. "Problem of Backward Proton Production," *Physical Review C*, **33**, 260 (1986)

Kikuchi, K.; Kawai, M. *Nuclear Matter and Nuclear Reactions*, John Wiley & Sons, Inc. (1968)

Madey, R.; Varga, J.; Baldwin, A.R.; Anderson, B.D.; Cecil, R.A.; Fai, G.; Tandy, P.C.; Watson, J.W. "Inclusive Neutron Spectra at 0° From the Reactions  $\text{Pb}(\text{Ne},n)\text{X}$  and  $\text{NaF}(\text{Ne},n)\text{X}$  at 390 and 790 MeV per Nucleon," *Physical Review C*, **38**, 184 (1985)

Menzel, H.; O'Sullivan, D.; Beck, P.; Bartlett, D.; "European Measurements of Aircraft Crew Exposure to Cosmic Radiation," *Health Physics*, **79**, 563 (2000)

Moritz, C. Current Biography Yearbook 1963, The H.W. Wilson Company (1963)  
Nagamiya, S.; Lemaire, M.-C.; Moeller, E.; Schnetzer, S; Shapiro, G.; Steiner, H.;  
Tanihata, I. "Production of pions and light fragments at large angles in high-energy  
nuclear collisions," *Physical Review C*, **24**, 971 (1981)

National Council on Radiation Protection and Measurement (NCRP), "Radiation  
Exposure and High-Altitude Flight," NCRP Commentary No. 12 (1995)

Schwarzschild, A.; Zupančič, Č; *Physical Review*, **129**, 854 (1963)

Simonsen, L.C.; Nealy, J.E. "Radiation Protection for Human Missions to the Moon and  
Mars," NASA Technical Paper No. TP-3079 (1991)

Townsend, L.W.; Wilson, J.W. "Energy-Dependent Parameterization of Heavy-Ion  
Absorption Cross Sections," *Radiation Research*, **106**, 283 (1986)

Townsend, L.W.; Nealy, J.E.; Wilson, J.W.; Simonsen, L.C. "Estimates of Galactic  
Cosmic Ray Shielding Requirements During Solar Minimum," NASA Technical  
Memorandum No. TM-4167 (1990)

Tuve, C. et al. "Neutron production at 0° from the  $^{40}\text{Ca} + \text{H}$  reaction at  $E_{\text{lab}} = 357\text{A}$  and  
 $565\text{ A MeV}$ ," *Physical Review C*, **56**, 1057 (1997)

Waters, M; Bllom, T.F.; Grajewski, B. "The NIOSH/FAA Working Women's Health  
Study: Evaluation of the Cosmic-Radiation Exposures of Flight Attendants," *Health  
Physics*, **79**, 553 (2000)

Weisskopf, V.F.; Ewing, D.H. "On the Yield of Nuclear Reactions with Heavy  
Elements," *Physical Review*, **57**, 472 (1940)

Wilson, J.W.; Townsend, L.W.; Chun, S.Y.; Buck, W.W.; Khan, F.; Cucinotta, F.;  
"BRYNTRN: A Baryon Transport Computer Code – Computation Procedures and Data  
Base," NASA Technical Memorandum No. TM 4037 (1988)

## **Appendices**

**Appendix A**  
**Abrasion Theory**  
**(From Cucinotta, 1997)**

In the Glauber model the scattering operator for nucleus-nucleus collisions is  
(Glauber 1970, Cucinotta 1994b)

$$f = \frac{iK}{2\pi} \int d^2b \exp(i\mathbf{q} \cdot \mathbf{b}) \Gamma(\mathbf{b}) \quad (\text{A1})$$

where  $K$  is the relative wave number of the projectile target,  $\mathbf{b}$  is the impact parameter, and  $\mathbf{q}$  is the momentum transfer. The profile function representing the multiple-scattering series at high energies is

$$\Gamma(\mathbf{b}) = 1 - \prod_{\zeta, j} [1 - \Gamma_{\zeta, j}(\mathbf{b} - \mathbf{s}_\alpha - \mathbf{s}_j)] \quad (\text{A2})$$

where  $\zeta$  and  $j$  label the target and projectile constituents, respectively. In equation (A2),  $\Gamma_{\zeta, j}$  is the two-body profile function with the internal coordinate having components  $\mathbf{r} = (\mathbf{s}, z)$  and represents individual nucleon-nucleon collisions occurring during the interaction of the nuclei.

The scattering amplitude of equation (A1) is related to the production cross section for a projectile nucleon from the abrasion (knockout) process by

$$\begin{aligned} \frac{d\sigma}{d\mathbf{k}} = & \sum_X \frac{1}{(2\pi)^2} \int dE_F \cdot d^2q d^2b d^2b' \exp[i\mathbf{q} \cdot (\mathbf{b} - \mathbf{b}')] \delta(E_i - E_f) \\ & \times \prod_{j=2}^n \left[ \frac{d\mathbf{k}_j}{(2\pi)^3} \right] \left\langle TP \middle| \Gamma^\dagger(\mathbf{b}') \middle| X F^* \mathbf{k}_j \right\rangle \left\langle \mathbf{k}_j F^* X \middle| \Gamma(\mathbf{b}) \middle| PT \right\rangle \end{aligned} \quad (\text{A3})$$

where  $\mathbf{k}_j$  denotes the wave numbers of the abraded nucleons,  $F^*$  denotes the prefragment (with  $A_{F^*} = A_P - n$ ), and initial and final states have been inserted into equation (A3).

Next, the change in energy of the target from the collision is as follows:

$$E_T - E_X = E_T - \sqrt{(\mathbf{p}_T - \mathbf{q})^2 + M_X^2} = E_T \left( 1 - \sqrt{\frac{q^2 + M_X^2 - M_T^2}{E_T^2}} \right) \quad (\text{A4})$$

where  $M_T$  and  $M_X$  are the target masses for the initial and final state, respectively. After closure on the final target states,

$$\frac{d\sigma}{d\mathbf{k}} = \frac{1}{(2\pi)^2} \int dE_{F*} d^2q d^2\mathbf{b} d^2\mathbf{b}' \exp[i\mathbf{q} \cdot (\mathbf{b} - \mathbf{b}')] \sigma_n(\mathbf{b}, \mathbf{b}', \mathbf{k}, \mathbf{q}, E_{F*}) \quad (\text{A5})$$

where

$$\sigma_n(\mathbf{b}, \mathbf{b}', \mathbf{k}, \mathbf{q}, E_{F*}) = \left\langle T \left| \int \prod_{j=2}^n \left[ \frac{d\mathbf{k}_j}{(2\pi)^3} \right] \delta(E_i - E_f) \left\langle P \left| \Gamma^\dagger(\mathbf{b}') \right| F^* \mathbf{k}_j \right\rangle \left\langle \mathbf{k}_j F^* \right| \Gamma(\mathbf{b}) \left| P \right\rangle \right| \right\rangle \quad (\text{A6})$$

To consider the energy conservation term  $\delta(E_i - E_f)$  in equation (6) above, use the Fourier transform pair

$$\sigma_n(t) = \int dE \exp(-iEt) \sigma_n(E) \quad (\text{A7})$$

and

$$\sigma_n(E) = \int \frac{dt}{2\pi} \exp(iEt) \sigma_n(t) \quad (\text{A8})$$

In the projectile rest frame, we have

$$E_i - E_f = S_n - T_{F*} + E_T - E_X - \sum_{j=1}^n \frac{\mathbf{k}_j^2}{2m_N} = \bar{E} - \sum_{j=w} \frac{\mathbf{k}_j^2}{2m_N} \quad (\text{A9})$$

where  $S_n$  is the separation energy and  $T_{F*}$  is the recoil energy of the prefragment (including excitation energy).

From Eqs. (A6), (A7) and (A9),

$$\sigma_n(t) = \langle T | \left\{ \prod_{j=2}^n \left[ \frac{d\mathbf{k}_j}{(2\pi)^3} \right] \exp(-i \sum_{j=1} \frac{\mathbf{k}_j^2 t}{2m_N} \langle P | \Gamma^\dagger(\mathbf{b}') | F^* \mathbf{k}_j \rangle \langle \mathbf{k}_j F^* | \Gamma(\mathbf{b}) | P \rangle) \right\} | T \rangle \quad (A10)$$

To simplify, first factor the profile function into projectile participant and spectator terms as

$$\Gamma(\mathbf{b}) = 1 - \prod_{l=n+1}^{A_p} Q_l(\mathbf{b} - \mathbf{s}_l) \prod_{j=1}^n Q_j(\mathbf{b} - \mathbf{s}_j) \quad (A11)$$

where

$$Q_j = \prod_{\zeta=1}^{A_T} (1 - \Gamma_{\zeta,j}) \quad (A12)$$

where  $Q(\mathbf{b} - \mathbf{s})$  is optically averaged over target coordinates.

If the prefragment mass is much greater than that of the knockouts, the projectile wave function can be factored as

$$|P\rangle = |F\rangle |\phi_n\rangle \quad (A13)$$

where  $|F\rangle$  and  $|\phi_n\rangle$  are the wave functions of the spectators (core) and participants (knockouts) respectively. Using plane wave states for  $|\mathbf{k}_j\rangle$  and substituting equations (A11) and (A13) into equation (A10), we obtain

$$\begin{aligned} \sigma_n(t) = & \langle T | \left\{ \binom{A_p}{n} \langle F | \prod_l Q_l^\dagger(\mathbf{b}' - \mathbf{s}_l') | F^* \rangle \langle F^* | \prod_l Q_l(\mathbf{b} - \mathbf{s}_l) | F \rangle \int d\mathbf{r}_1 d\mathbf{r}_1' \exp(i\mathbf{k} \cdot \mathbf{x}_1) Q_1^\dagger(\mathbf{b}' - \mathbf{s}_1') Q_1(\mathbf{b} - \mathbf{s}_1) \right\} \\ & \times \prod_{j=2}^n \left[ \int \frac{d\mathbf{k}_j}{(2\pi)^3} d\mathbf{r}_j d\mathbf{r}_j' \exp(i\mathbf{k}_j \cdot \mathbf{x}_j) \exp\left(\frac{-k_j^2 t}{2m_N}\right) Q_j^\dagger(\mathbf{b}' - \mathbf{s}_j') Q_j(\mathbf{b} - \mathbf{s}_j') \right] \phi_n^\dagger(\mathbf{r}_1', \dots, \mathbf{r}_n') \phi_n(\mathbf{r}_1, \dots, \mathbf{r}_n) \end{aligned} \quad (A14)$$

where  $\mathbf{x}_j = \mathbf{r}_j - \mathbf{r}'_j$ . Using the coherent approximation for the target wave function in the intermediate states and the independent particle model for the fragment wave function leads to the following equation:

$$\sigma_n(t) = \binom{A_p}{n} \mathcal{P}^{A_p-n}(\mathbf{b}, \mathbf{b}') \Lambda_{n-1}(\mathbf{b}, \mathbf{b}', t) \frac{dN_1}{d\mathbf{k}} \quad (\text{A15})$$

where the function  $\mathcal{P}(\mathbf{b}, \mathbf{b}')$  describes the projectile spectators as given by

$$\mathcal{P}^{A_p-n}(\mathbf{b}, \mathbf{b}') = \left\langle TF \left| \prod_l Q_l^\dagger(\mathbf{b}' - \mathbf{s}_l') \right| F^* \right\rangle \left\langle F^* \left| \prod_l Q_l(\mathbf{b} - \mathbf{s}_l) \right| FT \right\rangle \quad (\text{A16})$$

After performing closure in equation (A16), we find that

$$\mathcal{P}^{A_p}(\mathbf{b}, \mathbf{b}') = \left\langle TF \left| \prod_l Q_l^\dagger(\mathbf{b}' - \mathbf{s}_l') \prod_l Q_l(\mathbf{b} - \mathbf{s}_l) \right| FT \right\rangle \quad (\text{A17})$$

In equation (A15) we have defined

$$\frac{dN_1}{d\mathbf{k}} = \frac{1}{(2\pi)^3} \int d\mathbf{r} d\mathbf{r}' \exp(i\mathbf{k} \cdot \mathbf{x}) \rho(\mathbf{r}, \mathbf{r}') Q_l^\dagger(\mathbf{b}' - \mathbf{s}') Q_l(\mathbf{b} - \mathbf{s}) \quad (\text{A18})$$

where  $\rho(\mathbf{r}, \mathbf{r}') = \phi^\dagger(\mathbf{r}') \phi(\mathbf{r})$  is the one-body density matrix of the projectile. Next, from equation (A14), after evaluation of the integrals over  $\mathbf{k}_j$  for  $j > 2$ , and transforming back to energy space, we find that

$$\begin{aligned} \Lambda_{n-1}(\mathbf{b}, \mathbf{b}', T_{F*}, \mathbf{k}) &= \left\langle T \left| \prod_{j=2}^n d\mathbf{r}_j d\mathbf{r}'_j \rho(\mathbf{r}_j, \mathbf{r}'_j) Q_j^\dagger(\mathbf{b}' - \mathbf{s}'_j) \right. \right. \\ &\times \frac{m_N}{2} \left( \frac{1}{2\pi} \right)^{\frac{3(n-1)}{2}} \frac{\xi_{n-1}^{\frac{3(n-1)}{2}-1}}{\bar{x}_{n-1}^{\frac{3(n-1)}{2}-1}} J_{\frac{3(n-1)}{2}-1}^{(1)}(\xi_{n-1} x_{n-1}) \left| T \right\rangle \end{aligned} \quad (\text{A19})$$

where

$$\xi_{n-1} = \sqrt{2m_N \left[ T_{F*} + \frac{\mathbf{k}^2}{2m_N} - S_n - (E_T - E_X) \right]} \quad (\text{A20})$$

and

$$\bar{x}_{n-1} = \sqrt{\sum_{j=2}^n x_j^2} \quad (\text{A21})$$

and where  $J_m^{(1)}$  is the cylindrical Bessel function of the first kind of order  $m$ .

For  $n=1$ , we have  $\Lambda_0 = \delta(T_{F^*})$ . If we assume forward-peaked density matrices (about), a small argument expansion of the Bessel functions can be developed (#ref) that results in

$$\Lambda_{n-1}(\mathbf{b}, \mathbf{b}', T_{F^*}, \mathbf{k}) \approx C_{n-1} \left[ T_{F^*} + \frac{\mathbf{k}^2}{2m_N} - S_n - (E_T - E_X) \right]^{(n-1)} \Lambda_1^{n-1} \left( \mathbf{b}, \mathbf{b}', \frac{\xi_{n-1}}{\sqrt{n-1}} \right) + O(\xi^4 x^4) \quad (\text{A22})$$

where, for example,  $C_1 = 1$ ,  $C_2 = \frac{\pi}{4}$ ,  $C_3 = \frac{\pi}{105}$ , and  $C_4 = \frac{\pi^2}{204}$ .

The nucleon momentum distribution from abrasion then takes the following form:

$$\left( \frac{d\sigma}{d\mathbf{k}} \right)_{\text{abr}} = \sum_n \binom{A_p}{n} \frac{1}{(2\pi)^2} \int d^2 q d^2 b d^2 b' \exp[iq \cdot (\mathbf{b} - \mathbf{b}')] \mathcal{P}^{A_p - n}(\mathbf{b}, \mathbf{b}') \frac{dN_1}{d\mathbf{k}} \int dT_{F^*} \Lambda_{n-1}(\mathbf{b}, \mathbf{b}', T_{F^*}, \mathbf{k}) \quad (\text{A23})$$

If

$$q^2 + M_T^2 - M_X^2 \ll E_T^2 \quad (\text{A24})$$

then equation (A23) can be approximated by

$$\left( \frac{d\sigma}{d\mathbf{k}} \right)_{\text{abr}} = \sum_n \binom{A_p}{n} \int d^2 b \mathcal{P}^{A_p - n}(\mathbf{b}) \frac{dN_1}{d\mathbf{k}} \int dT_{F^*} \Lambda_{n-1}(\mathbf{b}, T_{F^*}, \mathbf{k}) \quad (\text{A25})$$

To include the final-state interaction of the nucleon knockouts, use the Eikonal model described elsewhere (Cucinotta 1994b). In this model, the plane waves are replaced by the distorted wave for the nucleon-projectile recoil interaction evaluated at

the relative energy between the knockout and the recoil. Modifying equation (A18) as in reference (Cucinotta, 1994b) gives

$$\frac{dN_1}{d\mathbf{k}} = \frac{1}{(2\pi)^3} \int d\mathbf{r} d\mathbf{r}' \exp(i\mathbf{k} \cdot \mathbf{x}) \rho(\mathbf{r}, \mathbf{r}') \exp[-2 \operatorname{Im} \chi^{(-)}(y)] Q_l^\dagger(\mathbf{b}' - \mathbf{s}') Q_l(\mathbf{b} - \mathbf{s}) \quad (\text{A26})$$

where  $\chi^{(-)}$  is the outgoing Eikonal phase. Equation (A26) ignores off-shell effects but includes the energy dependence of the final-state interaction and assumes a medium modified interaction, as described in reference (Cucinotta, 1994b).

The optical limit of the profile functions may be used for  $A_p A_T \gg 1$  (Glauber, 1970; Cucinotta, 1992), which gives us

$$\mathcal{P}^{A_p}(\mathbf{b}, \mathbf{b}') = \exp\{i[\chi(\mathbf{b}) - \chi^\dagger(\mathbf{b}')]\} \quad (\text{A27})$$

where the Eikonal phase is

$$\chi(\mathbf{b}) = \frac{A_p A_T}{(2\pi k_{NN})} \int d^2 q \exp(i\mathbf{q} \cdot \mathbf{b}) F_p(q) F_T(q) f_{NN}(q) \quad (\text{A28})$$

with  $F(q)$  denoting the one-body form factor and  $f_{NN}$  denoting the two-body scattering amplitude, which we represent by

$$f_{NN} = \frac{\sigma_{NN}(\alpha + i)k_{NN}}{4\pi} \exp\left(-\frac{1}{2} Bq^2\right) \quad (\text{A29})$$

where  $\sigma_{NN}$  is the two-body total cross section,  $k_{NN}$  is the relative momentum in the two-body center of mass frame,  $B$  is the two-body slope parameter, and  $\alpha$  the ratio of the real to imaginary parts of  $f_{NN}(\mathbf{q} = 0)$ . For inelastic terms, we write in the optical limit (Cucinotta, 1992) that

$$Q_j^\dagger(\mathbf{b}' - \mathbf{s}_j') Q_j(\mathbf{b} - \mathbf{s}_j) = \exp[\tilde{\Omega}(\mathbf{b}' - \mathbf{s}_j', \mathbf{b} - \mathbf{s}_j)] - 1 \quad (\text{A30})$$

with

$$\tilde{\Omega}(\mathbf{b}' - \mathbf{s}_j', \mathbf{b} - \mathbf{s}_j) = \frac{1}{(2\pi k_{NN})^2} \sum_{\alpha} \int d^2 q d^2 q' \exp[i\mathbf{q} \cdot (\mathbf{b} - \mathbf{s}_j + \mathbf{s}_{\alpha})] \exp[-i\mathbf{q} \cdot (\mathbf{b}' - \mathbf{s}_j' + \mathbf{s}_{\alpha})] f_{NN}^{\dagger}(\mathbf{q}') f_{NN}(\mathbf{q}) \quad (A31)$$

The one-body density matrix is evaluated using a local density approximation, which is assumed to factor as:

$$\rho(\mathbf{r}, \mathbf{r}') \approx \rho(\mathbf{y}) n(\mathbf{x}) \quad (A32)$$

with  $\mathbf{x} = \mathbf{r} - \mathbf{r}'$  and  $\mathbf{y} = .5(\mathbf{r} + \mathbf{r}')$  and where the one-body density is given by the diagonal part of the density matrix

$$\rho(\mathbf{r}) \approx \rho(\mathbf{r}, \mathbf{r}'), \quad (\mathbf{r}' = \mathbf{r}) \quad (A33)$$

and  $n(\mathbf{x})$  is the Fourier transform of the nucleon momentum distribution

$$n(\mathbf{x}) = \int d\mathbf{p} \exp(i\mathbf{p} \cdot \mathbf{x}) n(\mathbf{p}) \quad (A34)$$

where  $n(\mathbf{p})$  is defined by

$$n(\mathbf{p}) = \int d\mathbf{r} d\mathbf{r}' \exp(-i\mathbf{p} \cdot \mathbf{x}) \rho(\mathbf{r}, \mathbf{r}') \quad (A35)$$

with normalization

$$\int n(\mathbf{p}) \frac{d\mathbf{p}}{(2\pi)^3} = 1 \quad (A36)$$

The one-body density and the nucleon momentum distribution at small to modest values of  $\mathbf{p}$  are known from electron scattering. For large values of  $p$ , backward production of protons suggests that large enhancements to the nucleon momentum distribution result from correlation effects when compared with predictions of independent-particle models. In addition, this enhancement is largely independent of nuclear mass.

Haneishi and Fujita (Haneishi, 1986) have introduced the following momentum distribution:

$$n(\mathbf{p}) = n_0 \sum_{i=1}^3 C_i \exp\left(-\frac{p^2}{2p_i^2}\right) \quad (\text{A37})$$

where  $n_0$  is a normalization constant. The last term in equation (A37) is expected to directly reflect the nuclear correlations. The value of  $C_3 = 0.003$  used in (Haneishi, 1986) was found to be too large in (Cucinotta, 1994a; Cucinotta, 1994b); thus the value of  $C_3$  in (Cucinotta, 1997) was set at 0.0008.

**Appendix B**  
**Coalescence Subroutine**

The following FORTRAN 77 subroutine was used in the determination of the coalescence-reduced neutron production cross sections discussed in chapter 4. Please note that the real\*16 type declaration and the qsqrt function call may not be available in all FORTRAN 77 implementations.

```

c**SUBROUTINE COAL(iat,iap,izt,izp,adeg,tnnlab,ds_total,linvt,eel,ne)**
c this subroutine calculates a reduction of the neutron production cross
c sections due to coalescence based on equations by Awes, Nagamiya, and Gutbrod
c returns: ds_total
c called by: ubernspec
c calls: none

SUBROUTINE COAL(iat,iap,izt,izp,adeg,tnnlab,ds_total,linvt,eel,ne)
implicit none
real*8 pi,r0,rf2,sigma0,eel(50),f,beta,delta,nucleon_mass,
&proton_factor,p0,adeg,plab(50),temp_total,ds_total(50),linvt(50),
&gamma,tnnlab
real*16 k(4),rf1,r,s,t,u,q,n_obs1,n_obs2,eterm,elab,p_obs1,term1,
&term2,term3,root,parta,p_total,p_total2,partb,inner
integer iat,iap,izt,izp,a,z,n,target_neuts,proj_neuts,ie,ne,i

PI=4.*DATAN(1.D0)
target_neuts=iat-izt
proj_neuts=iap-izp
nucleon_mass=.9386
r0=1.26

c proton_factor will be used to convert neutron cross sections to protons
proton_factor=(real(izt+izp))/(real(target_neuts+proj_neuts))

c sigma0 is a parameterized absorption cross section in two forms:
c the nucleon-nucleus form is due to Wilson et. al. 1988
c the nucleus-nucleus form is due to Townsend et. al. 1986
if((iat.eq.1).or.(iap.eq.1)) then
  f=1-0.62*Exp(-tnnlab/200)*Sin(10.9*tnnlab**(-.28))
  if(iat.eq.1) then
    sigma0=f*45.*real(iap)**.7*(1.+0.016*Sin(5.3-2.63*Log
    &(real(iap))))
  else
    sigma0=f*45.*real(iat)**.7*(1.+0.016*Sin(5.3-2.63*Log
    &(real(iat))))

```

```

    end if
else
  beta=1.+5./tnnlab
  delta=0.2+1./real(iap)+1./real(iat)-0.292*Exp(-tnnlab/
&792.)*Cos(0.229*tnnlab**0.453)
  inner=(real(iap)**(1./3.)+real(iat)**(1./3.)-delta)
  sigma0=10.*pi*(r0**2)*beta*(inner**2)
end if

c now start looping through energies and values
do 10 ie=1,ne
  elab=.001*eel(ie)
  p_total=linvt(ie)
  print *, ' '
  print *, 'ie',ie,'p_total',p_total

c now set up cases for each fragment of interest
c 1=deuteron, 2=triton, 3=helion, 4=alpha
c p0 is the coalescence radius for the resultant nuclei (MeV/c)
c these are approximations of those used in Gutbrod et. al
c   deut_p0=125
c   trit_p0=129
c   helion_p0=129 (observed production of helions is lt tritons)
c   alpha_p0=140
c these values are from Awes et. al. (1981); helion interpolated
c   deut_p0=170
c   trit_p0=215
c   helion_p0=240 (approx)
c   alpha_p0=270
c Nagamiya et. al. (1981) suggested p0 of ~90

do 20 i=1,4
  select case(i)
    case(1)
      z=1
      n=1
      a=2
      p0=.09
    case(2)
      z=1
      n=2
      a=3
      p0=.09
    case(3)
      z=2

```

```

n=1
a=3
p0=.09
case(4)
z=2
n=2
a=4
p0=.09
end select
gamma=1+elab/nucleon_mass
k(i)=(a/(z*n))*proton_factor**z*(4.*pi*p0**3./(3.*sigma0*
&nucleon_mass))**(a-1)
if(ie.eq.1)print *, 'i',i,'k(i)',k(i)
20  continue

```

c now set up cases for each fragment of interest  
c r=deuteron, s=triton, t=helion, u=alpha

```

r=k(1)
s=k(2)
t=k(3)
u=k(4)
q=s+t

```

c this section solves the following cubic equation:

```

c  p_total=p_obs1+r*p_obs**2+q*p_obs**3 for p_obs given p_total
c neglecting the (very small) alpha term. Solving the fourth order
c polynomial is not unreasonably complex in itself, but fortran doesn't
c like to work with the cube root of a negative number - wants to make a
c complex number out of it. The error is very, very small until you get
c to extremely large (~10**7 mb) cross section, then grows slowly
parta=qsqrt(27.*q**2*p_total**2-r**2*(1.+4.*r*p_total)+q*
&(4.+18.*r*p_total))
partb=(2.*r**3-27.*q**2*p_total+3.*q*(-3.*r+sqrt(3.)*
&parta))**1./3.
p_obs1=-(2.*r-(2.*2.**1./3.)*(3.*q-r**2))/partb+2.**2./3.
&)*partb)/(6.*q)

```

c these are the two reduction factors - rf1 is based on the calculated  
c coefficients using the total production cross sections, rf2 is based  
c on the parameterized coefficients used to calculate the observed cross  
c sections. At present, rf2 is used. It is possible to use the  
c calculated coefficients in the solution for the observed cross sections.  
c However, the results should differ only slightly.

```

rf1=(1.-r*p_total-(s+t)*p_total**2-u*p_total**3)

```

```
rf2=p_obs1/p_total
print *,'rf2',rf2
ds_total(ie)=rf2*ds_total(ie)
print *,'p_obs1',p_obs1,'d after (rf2)',ds_total(ie)
10 continue

return
end
```

**Appendix C**  
**Additional Plots**  
**75 MeV per nucleon C+Al**

Table C.1 Chi-squared goodness of fit check for previous and current models. Bold type indicates best fit.

Lab Angle (degrees)	$p_o$ MeV/c	$\chi^2$		
		E<T	E>T	All Data
10°	90	<b>188</b>	1143	1331
	125	345	<b>402</b>	<b>747</b>
30°	90	18731	102880	121611
	125	<b>10040</b>	<b>56773</b>	<b>66814</b>
45°	90	6657	30849	37506
	125	<b>5293</b>	<b>23100</b>	<b>28393</b>
60°	90	110	289	398
	125	<b>60</b>	<b>264</b>	<b>324</b>
90°	90	42709	no data	42708
	125	<b>30713</b>	no data	<b>30713</b>
125°	90	<b>43389</b>	no data	<b>43389</b>
	125	52807	no data	52807

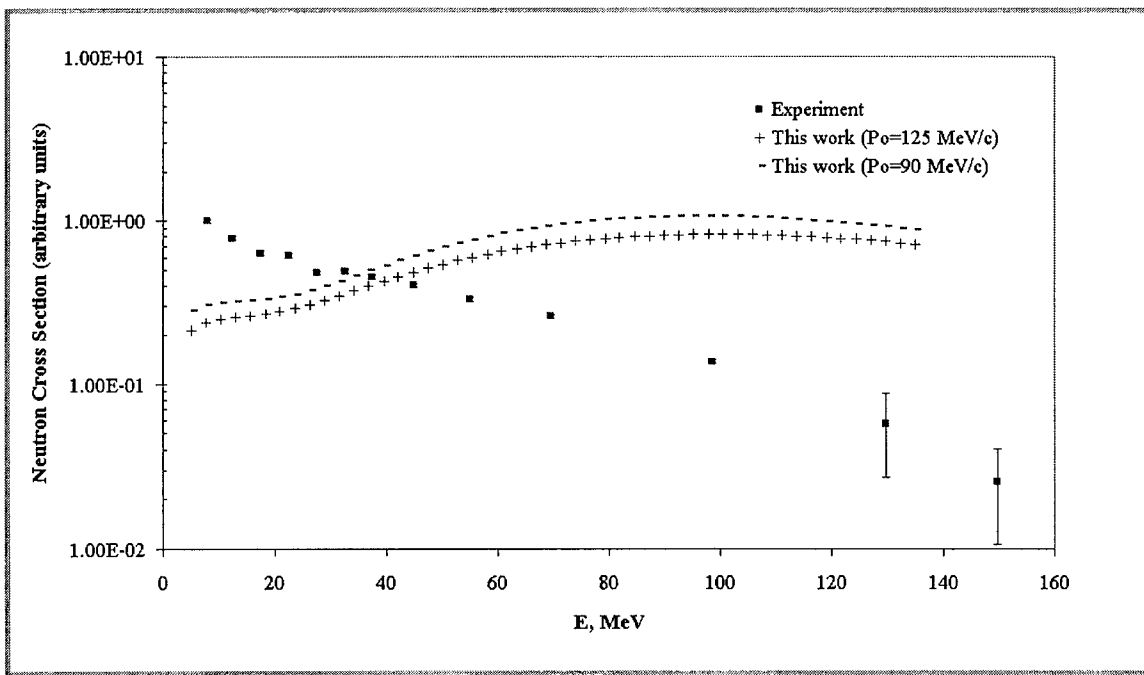


Figure C.1 Comparison of results for 75 MeV per nucleon C+Al at 30° lab angle

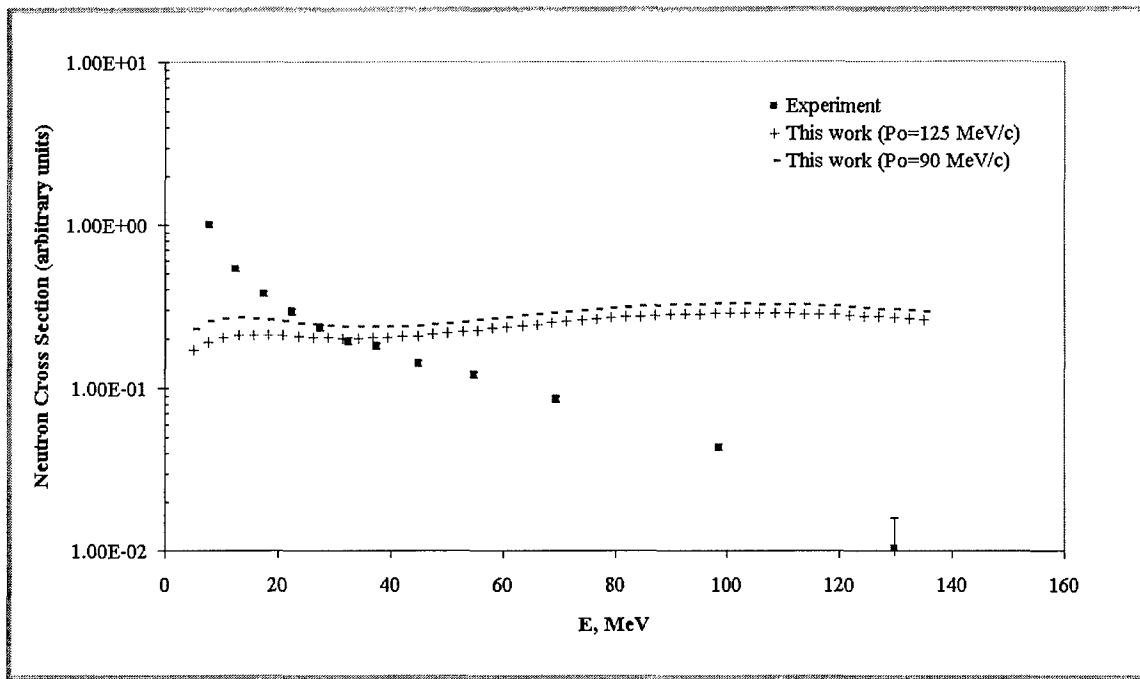


Figure C.2 Comparison of results for 75 MeV per nucleon C+Al at 45° lab angle

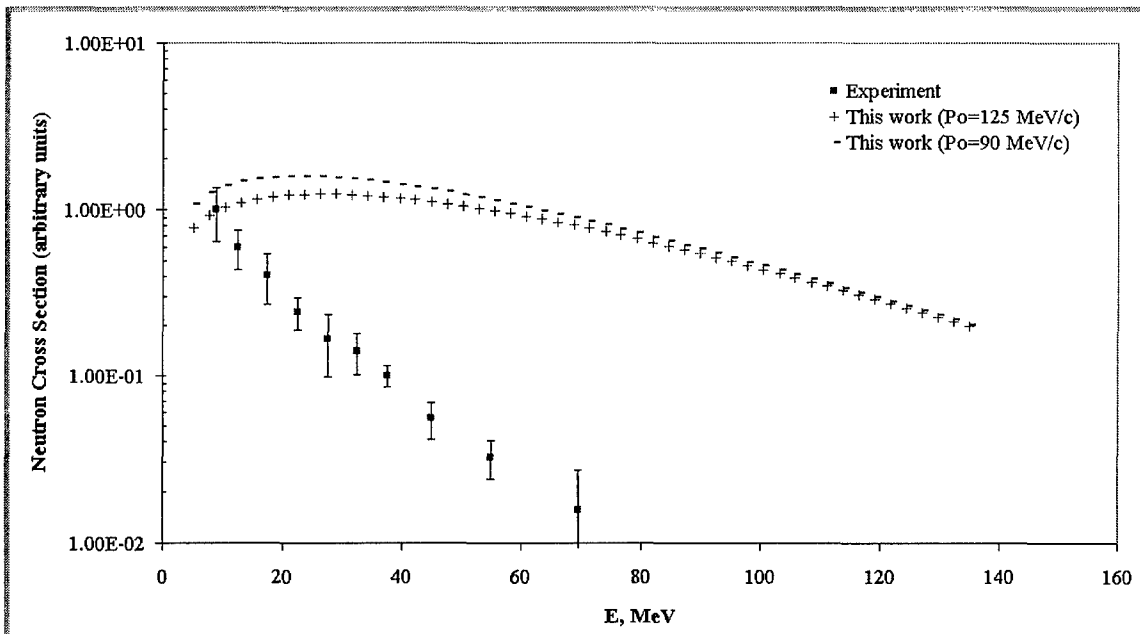


Figure C.3 Comparison of results for 75 MeV per nucleon C+Al at 90° lab angle